All Theses and Dissertations

2014-07-01

Elastic Energy Absorption via Compliant Corrugations

Sean S. Tolman
Brigham Young University - Provo

Elastic Energy Absorption via Compliant Corrugations

Sean S. Tolman

A dissertation submitted to the faculty of
Brigham Young University
in partial fulfillment of the requirements for the degree of

Doctor of Philosophy

Larry L. Howell, Chair
Anton E. Bowden
Spencer P. Magleby
David T. Fullwood
Matthew K. Seeley

Department of Mechanical Engineering

Brigham Young University

June 2014

ABSTRACT

Elastic Energy Absorption via Compliant Corrugations

Sean S. Tolman
Department of Mechanical Engineering, BYU
Doctor of Philosophy

Elastic absorption of kinetic energy and distribution of impact forces are required in many applications. This may be achieved through the use of compliant corrugations. An innovative padding concept is investigated for such applications. Also, recent attention given to the potential for using origami in engineering applications may provide new corrugation configurations that are advantageous for energy absorption and force distribution. This work explores three areas related to these concepts.

First, the parameters of a compliant, corrugated padding concept are investigated using Finite Element Analyses (FEA) and physical testing. The shape of the corrugation cross section is explored as well as the wavelength and amplitude by employing a full factorial design of experiments. FEA results are used to choose designs for prototyping and physical testing. The results of the physical testing were consistent with the FEA predictions although the FEA tended to underestimate the peak pressure compared to the physical tests. A performance metric is proposed to compare different padding configurations. The concept shows promise for sports padding applications. It may allow for designs which are smaller, more lightweight, and move better with an athlete than current technologies yet still provide the necessary protective functions.

Second, the elastic energy absorbing properties of a particular origami folding pattern, the Miura-ori, is investigated. Analytical models for the kinematics and force-deflection of a unit cell based on two different modes of elastic energy absorption are derived. The models are used to explore the effects of the key geometrical parameters of the tessellation. Physical prototypes are compared to the analytical models.

Third, a three-stage strategy is presented for selecting materials for origami-inspired corrugations that can deform to achieve a desired motion without yielding, absorb elastic strain energy, and be light weight or cost effective. Two material indices are derived to meet these requirements based on compliant mechanism theory. Using Finite element analysis, it is shown that the properties of Miura-ori pattern has advantages for energy absorption and force distribution when compared to a triangular wave corrugation. While the focus of these studies is the Miura-ori tessellation, the methods developed can be applied to other tessellated patterns used in energy absorbing or force distribution applications.

Keywords: energy absorption, compliant mechanism, origami, corrugation, material selection, Miura-ori

ACKNOWLEDGMENTS

TABLE OF CONTENTS

LIST OF TABLES

LIST OF FIGURES

CHAPTER 1.   INTRODUCTION

1.1   Motivation

Engineers often face the challenge of finding ways to manage and absorb kinetic energy. This occurs in applications such as protecting people from impacts in vehicle collisions, guarding athletes in sporting activities, defending soldiers during military operations, mitigating damage to equipment during operation, or safely transporting products. Factors that often determine the optimum design for a given application are the size, weight, and toughness (i.e. ability to absorb energy) of the final design. Also, it may be important in certain applications that the energy absorbing device be reusable. It would be impractical for a football player to have to replace his helmet after every tackle or impact. Innovations that provide reusable and efficient (in terms of size and/or weight) energy absorbing capabilities would be valuable to engineers facing such design challenges.

Corrugated materials have long been important for many structural engineering applications. A thin plate of galvanized steel can be made to support the load of snow on a roof without increasing its mass by simply forming it into a wave shape. Corrugations may also prove to be valuable as reusable energy absorbing materials if the corrugation is allowed to deflect elastically when impacted, thereby absorbing energy. Additionally, other corrugation configurations inspired by origami designs may provide even more energy absorbing potential than traditional one-dimensional corrugations. This research investigates the potential for creating innovative and efficient energy absorbing methods through the elastic deformation of compliant corrugations.

1.2   Objectives

The main objective of this research is to investigate elastic energy absorption via compliant corrugations. The corrugations that are studied are a sine-wave corrugation embedded in foam

and double corrugations related to the Miura-ori tessellation. The three research objectives are as follows:

1. Use dynamic, three dimensional, finite element analysis to understand the corrugation parameters of the corrugated padding concept that are well-suited for energy absorption and verify the analysis through the testing of physical prototypes.

2. Develop an analytical model based on spherical mechanism kinematics and the pseudo-rigid-body approach [1] to predict the motion and energy absorption characteristics for the Miura-ori unit cell.

3. Investigate material-related issues pertaining to the design of origami-based compliant corrugations for energy absorbing applications.

1.3 Overview

The research for the first objective is presented in Chapter 2. It is a study of an innovative padding design which consists of a compliant, corrugated sheet that is embedded in an elastic polymer foam. The concept was developed by two BYU Capstone teams, Cougar Armor (2009-2010) and Hephaestus Creations (2010-2011), and sponsored by XO Athletics. The main question that is answered is how the parameters of the cross-sectional wave shape of the corrugation (its period and amplitude) affect the energy absorbing properties of the padding. To answer this question, a combination of two- and three-dimensional quasi-static and dynamic Finite Element Analysis (FEA) together with physical testing was used. This manuscript was coauthored by Amanda Beatty, Anton Bowden and Larry Howell and is currently under review in the *Journal of Sports Engineering and Technology*.

An idea motivated by the research of the first objective was to study how other, more complex, corrugation configurations may be used for energy absorption. A specific area of origami design focuses on creating two- or three-dimensional repeating geometric patterns called tessellations. One well-known tessellation, the Miura-ori, is created when paper is folded to create a repeating pattern of parallelograms. The result is a corrugation comprised of two mutually orthogonal zig-zag waves. When a traditional, one-dimensional corrugation is subjected to a load

normal to the corrugated plane, the deflection of the wave is limited to the peaks where the force is applied. However, the Miura-ori forms an array of mechanisms which allow for the transfer of force and energy across the corrugation. This property may be advantageous for energy absorbing applications.

Presented in Chapter 3 are the results of the second research objective. It focuses on understanding how elastic energy is stored in a Miura-ori-based mechanism and what its force-deflection characteristics are. Kinematic and kinetic models were developed for a single unit cell based on two modes of energy storage. In one mode, energy is stored in the folds or hinges of the corrugation. In another mode, energy is stored in an elastic membrane which is stretched through the expanding motion of the corrugation. The models are used to explore the energy absorption effects of the geometric properties of the Miura-ori. They are also used to analyze data collected from the testing of physical prototypes. These models can serve as valuable design tools and their derivation as a useful approach for analyzing similar origami-inspired, compliant corrugations. This manuscript was coauthored by Spencer Magleby and Larry Howell.

The third objective, presented in Chapter 4, is the investigation of material-related issues pertaining to the design of origami-based compliant corrugations. It presents the analysis and development of a method for material selection based on key material properties relating to the mechanical performance of these corrugations. The method is a three-step process that begins with screening materials based on elastic strain and modulus values, which leads to the selection of a suitable subclass of material for compliant-mechanism-type applications. Second, the Ashby method [2] is used to provide an efficient means for refining the choice of material further by optimizing particular properties of the final component (such as mass, cost, resilience) within the applied engineering constraints. Third, specific stiffness characteristics are chosen to deliver improved force distribution and energy absorption properties for a peak desired force transfer. These characteristics can be achieved through a combination of detailed geometry and/or local material choice and are investigated in this study through FEA. The development of this method will be important in the transition of origami-inspired design from paper to other materials. This manuscript was coauthored by Isaac Delimont, David Fullwood, and Larry Howell and is currently under review in *Smart Materials and Structures*.

CHAPTER 2.   PARAMETER CHARACTERIZATION FOR ELASTIC ENERGY AB-SORPTION OF AN EMBEDDED CORRUGATED WAVE PADDING CONCEPT WITH SPORTS APPLICATIONS

2.1 Introduction

Suffering an injury is a major risk associated with participating in all levels of sports activities ranging from recreational participants up to elite professional athletes. The use of protective equipment such as padding has been shown to reduce some injuries to athletes [3–12]. Many organized sports have rules that require participants to use protective equipment such as helmets and padding in hopes of reducing the risk of certain injuries. Additionally, some athletes choose to wear discretionary protective equipment to provide further protection.

However, some athletes may prefer not to use protective equipment if they feel it will negatively affect their level of athletic performance. This was demonstrated in 2013 by the reactions of some professional football players to the decision of the National Football League in the United States to require thigh and knee pads for all players. One professional player was quoted as saying, "I don't want that at all. I don't like having anything restricting my movement in my legs" [13].

The main purpose of athletic protective padding is to absorb energy and distribute forces from impacts to the players. It is also desirable that the padding not inhibit the movement or negatively affect the performance of the athletes. Therefore, there continues to be a need to explore, evaluate and develop potential new designs for sports protective padding which are smaller, more lightweight, and move better with an athlete, yet still provide the necessary protective functions.

Corrugated plates are a familiar building and structural material that are used in numerous engineering applications ranging from decking and roofing to sandwich plate core structures. They are easy to form, cost-efficient and have a higher strength-to-weight ratio than flat plates [14]. Because of the widespread use of corrugated plates in engineering, much effort has been applied to understanding and modeling their characteristics. Shimansky and Lele [15] developed an analytical

4

model for the deformation of a sinusoidally corrugated plate subjected to a transverse load (in the plane of the plate and perpendicular to the normal of the cross section of the corrugation). Their model assumed small deflections. He et al. [16] analyzed corrugated-core, honeycomb-core and X-core using a semi-analytical method that was based on linear elastic, small deformation theory. Gilchrist [17] performed a large deformation finite element analysis of corrugated paper board. Many researchers proposed modeling corrugated plates and sandwich boards as equivalent orthotropic plates. The material properties for the orthotropic plate were determined by analyzing the corrugate analytically or numerically typically using finite elements [14, 18–28]. An overview of some of the most recent work done in energy absorbing properties of corrugated core and foam-filled corrugated core can be found in Zhang [29]. Most of the studies focus on the compressive strength and energy absorption mainly through plastic deformation of the corrugation. Little work has been done to study the compliant or elastic energy absorbing properties of a corrugated plate undergoing large deflection.

Elastic foam is a common material used for energy absorption in sports applications. The energy absorption of foam combined with other materials has been studied in the context of sports padding often with a particular emphasis on helmets and preventing head injuries [7, 10, 30, 31]. The analysis of foams using the finite element method can be challenging for dynamic impact analyses but is a valuable research and design tool for understanding such events [32, 33].

An innovative padding concept incorporating a compliant corrugation embedded in an elastic foam (Figure 2.1) holds potential interest for energy absorption and force distribution applications such as in athletic protective equipment. This is a patent-pending design developed with XO Athletics through the BYU Capstone senior design program. The ability of the corrugation to deflect and elastically absorb energy, combined with lateral energy dispersion through a surrounding foam matrix presents an intriguing engineering construct. The purpose of this work was to utilize FEA and physical prototype testing to explore how specific design parameters of the corrugated padding concept affect energy absorption and force distribution capability.

Figure 2.1: Concept for compliant corrugation embedded in foam.

2.2 Method

2.2.1 Corrugation Shape Analysis

The first aspect considered was how the shape of the corrugation affects its compliance and energy absorbing properties. A two-dimensional Finite Element Analysis (FEA) was performed for four different shapes. The beam shapes were designed to have equivalent amplitude and wavelength as if they were part of a repeating, corrugated wave. The shapes compared were: a sinusoidal curve, a simple arc, a triangular wave and a 3rd-order polynomial curve. The polynomial curve was designed to match the deflected shape of a cantilever beam with an end load as calculated using an elliptic integral solution. The shapes are shown in Figure 2.2. Beam elements were used and assigned the material properties of polycarbonate. One end of the wave was fixed and a vertical deflection load applied to the free end.

2.2.2 Sine Wave Parameter Analysis

The sinusoidal curve was used for further study to explore the effects of the corrugation amplitude and wavelength on its energy absorption and force distribution capability. A full factorial design of experiments (DOE) was employed using three levels for the two parameters, resulting in nine different designs for analysis. The DOE and corrugation parameters are shown in Table 2.1 where the configurations are designated by the relative wavelength and height (e.g. HiLo represents a high length or wavelength and a low corrugation height or amplitude). These designs

6
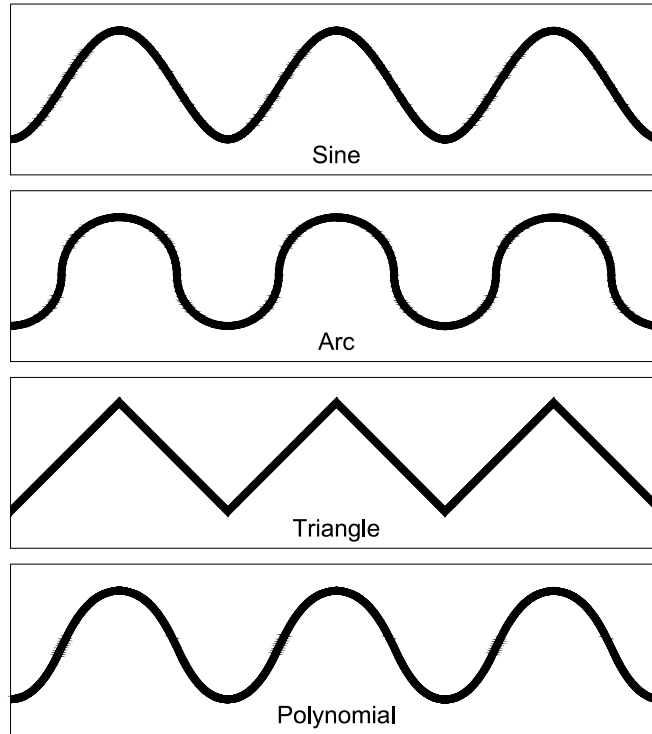
Figure 2.2: Corrugation shapes for 2D finite element analysis.

were evaluated using both quasi-static and dynamic three-dimensional FEA in LS-DYNA [34]. The two analyses predicted the padding response for a given deflection (quasi-static) and for a given energy (dynamic). The ranges for each parameter were chosen based on the materials and dimensions consistent with sports padding applications.
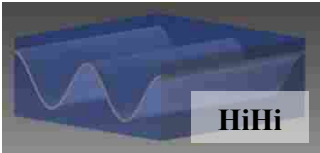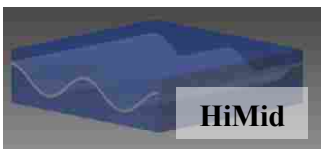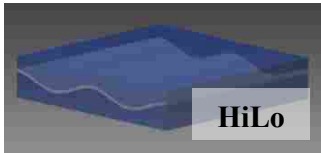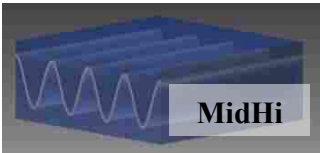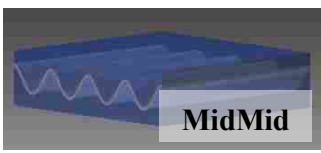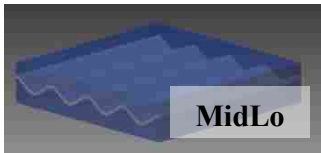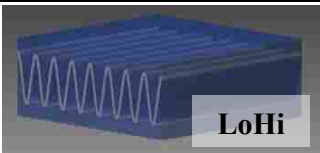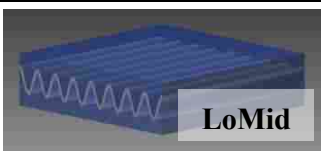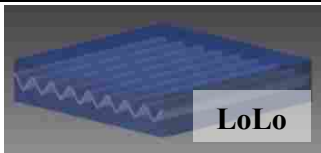
3D solid models of the geometry were created using Autodesk Inventor [35] and meshed using solid hexahedral elements in LS-PrePost [36]. The corrugations were modeled as sine waves with amplitude and wavelengths as defined in Table 2.1. Quarter symmetry was used to simplify the analysis. The material model used for the corrugation was MAT_ELASTIC (MAT_001) which is an isotropic, hypoelastic material. For the foam, MAT_LOW_DENSITY_FOAM (MAT_057) was used. This material model allows the user to define the material stiffness by entering a custom loading curve. The stress-strain behavior of the polyurethane foam was quasi-statically tested in compression to collect data for the loading curve. Symmetry boundary conditions were applied to two adjacent sides of the model and the nodes on the bottom face were constrained vertically. The nodes on the top and the other two sides were unconstrained. For the quasi-static analyses,

7

each model was compressed to 40% of its total thickness using a spherical, rigid wall. For the dynamic tests, a solid sphere was modeled and meshed in LS-PrePost and constrained to be rigid using MAT_RIGID (MAT_020). The size and velocity of the impacting sphere were chosen to simulate the parameters of a physical drop test that was designed to compare corrugated padding configurations. The parameters of the test are presented in the next section.

2.2.3 Physical Testing

The FEA results were used to guide the selection of three designs for prototyping and physical testing. These were the LoLo, LoMid and MidMid configurations. The corrugation in the padding was made by compression-molding 0.79 mm (1/32 in) thick polycarbonate. The molds were created by machining the corrugated shapes in aluminum using wire EDM. The mold was heated to 148-154 C (300-310 F), just above the glass transition temperature of polycarbonate. A 101 x 101 mm (4 x 4 in) piece of polycarbonate was placed between the two heated sides of the

Table 2.1: DOE for corrugation parameter study.

		Corrugation Height (2 x Amplitude)		
		High 12.7 mm (1/2 in)	**Mid** 6.35 mm (1/4 in)	**Low** 3.18 mm (1/8 in)
Length (Wavelength/2)	**High** 12.7 mm (1/2 in)	HiHi	HiMid	HiLo
	Mid 6.35 mm (1/4 in)	MidHi	MidMid	MidLo
	Low 3.18 mm (1/8 in)	LoHi	LoMid	LoLo
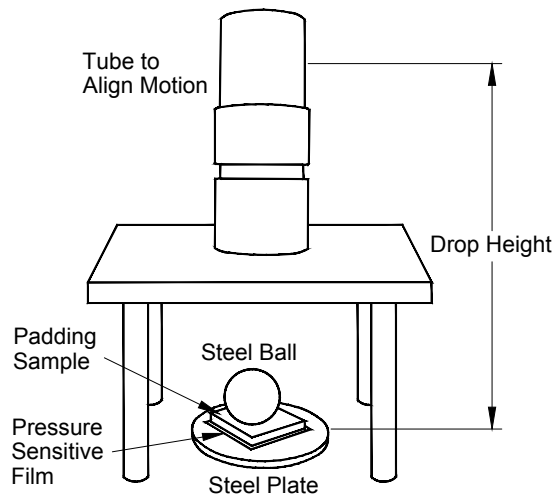
Figure 2.3: Apparatus for controlled drop testing.

mold, and the molds were pressed together with a pressure of 138 KPa (20 psi). The mold was left in this position until it was cooled so annealing would occur and remove the internal stresses. The foam surrounding the corrugation was a 192 kg/m (12 lb/ft) free rise density polyurethane foam. It is a two-part liquid foam that was hand mixed, then poured on the corrugated polycarbonate allowing 3.2 mm (0.125 in) of foam above and below the corrugation peaks. It then was left to solidify for at least an hour.

Controlled drop tests were conducted using the apparatus, shown in Figure 2.3, to drop a steel ball onto the padding prototypes. The test setup and parameters were based on previous tests done by Francisco et al. [37] which were designed to simulate low-velocity, soccer shin guard impacts. A 2 kg (4.5 lb) steel ball was dropped from a height of 50 cm (19.5 in) above the bottom of the test specimen. The resultant energy applied and absorbed by the padding was 9.7 J. A pressure sensitive film (Fujifilm) was placed beneath the padding and recorded the peak force and force distribution below the padding.

2.3 Results

2.3.1 2D Finite Element Analysis of Corrugation Shape

The 2D FEA of the four different corrugation shapes was used to compare the vertical force at the free end of each beam. The force-deflection characteristic of the shape is a key indicator of its energy absorption capability. As can be seen in Figure 2.4, the shape of the corrugation does not significantly affect its force-deflection characteristics.

2.3.2 3D Finite Element Analysis of Sine Wave Parameters

Both quasi-static and dynamic analyses were run on the 3D models to understand how the corrugation amplitude and wavelength affect the ability of the padding to absorb energy and distribute impact loads. Using the quasi-static analysis, the force-displacement data were integrated to get the work energy involved in deforming the foam and corrugation. Rather than comparing the total energy absorbed by each configuration, the energy absorbed for a given force in each model is compared. The energy was calculated by integrating the force deflection curve up to a force of 2.1 kN for each configuration. Also, since the weight of the padding is an important factor for sports applications, the energy was divided by the mass of the padding to show the specific energy or energy absorbed per unit mass of each model. This provides a measure of the energy-absorbing mass efficiency of the padding models and a means for comparing the configurations to understand the effects of the wave parameters. These data are presented in Figure 2.5 as a surface plot to visualize the corrugation parameter's effects on the normalized energy for a given force. It can be seen that generally, the normalized energy absorbed increases with the wavelength of the corrugation.

From the dynamic FEA, the acceleration pulse experienced by the sphere and the force distribution transferred through the padding were compared for each of the configurations defined in the DOE (Table 2.1). For managing impacts, it is desirable that the padding absorbs impact energy over a longer time duration and produces a smaller peak acceleration. Lower acceleration results in lower impact forces transferred to the athlete through the padding. Figure 2.6 shows a comparison of the acceleration pulses for each of the corrugation configurations based on the dynamic 3D FEA. The high amplitude configurations have a longer pulse and lower peak acceleration than the
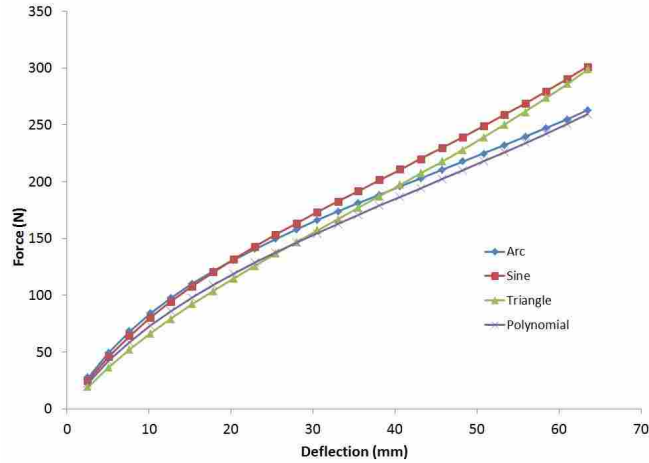
Figure 2.4: Results of 2D FEA showing beam end load for corrugation shapes.
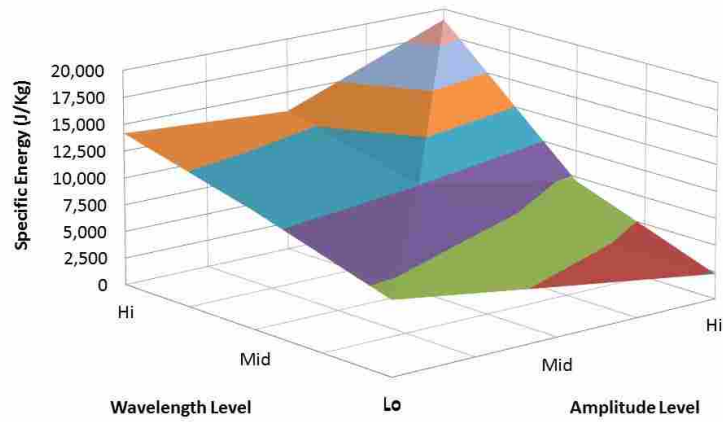
Figure 2.5: Energy for a given force normalized by mass based on quasi-static 3D FEA.

configurations with lower amplitudes. Also, reducing the wavelength of the corrugation tends to decrease the calculated peak acceleration.

The force distribution can be visualized by creating fringe or contour plots of the stress distribution in the bottom surface elements of the padding models. The force distributions of all nine configurations are shown in Figure 2.7. As with the acceleration, the configurations with the lowest peak stress and a more distributed stress are those with higher amplitude corrugation.

The deformation of the corrugation generally occurred as bending in the direction of the corrugation as shown in Figure 2.8. However, the LoHi and MidHi configurations exhibited a

11
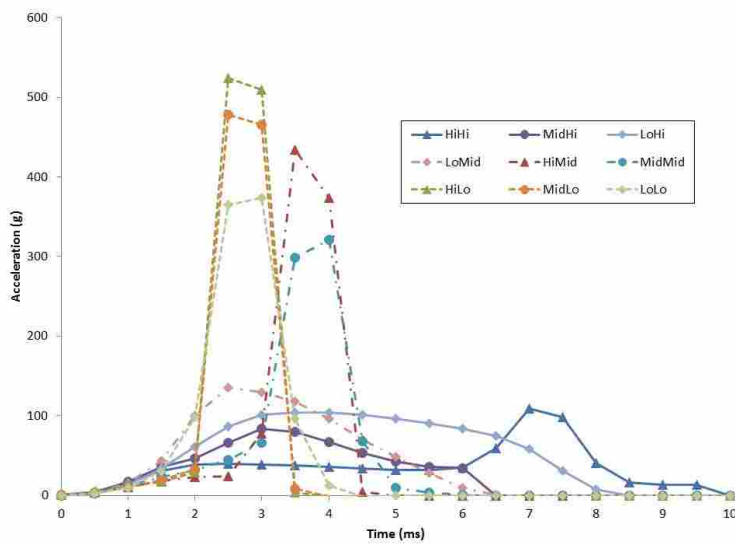
Figure 2.6: Acceleration pulse comparison of each corrugation configuration based on dynamic 3D FEA.
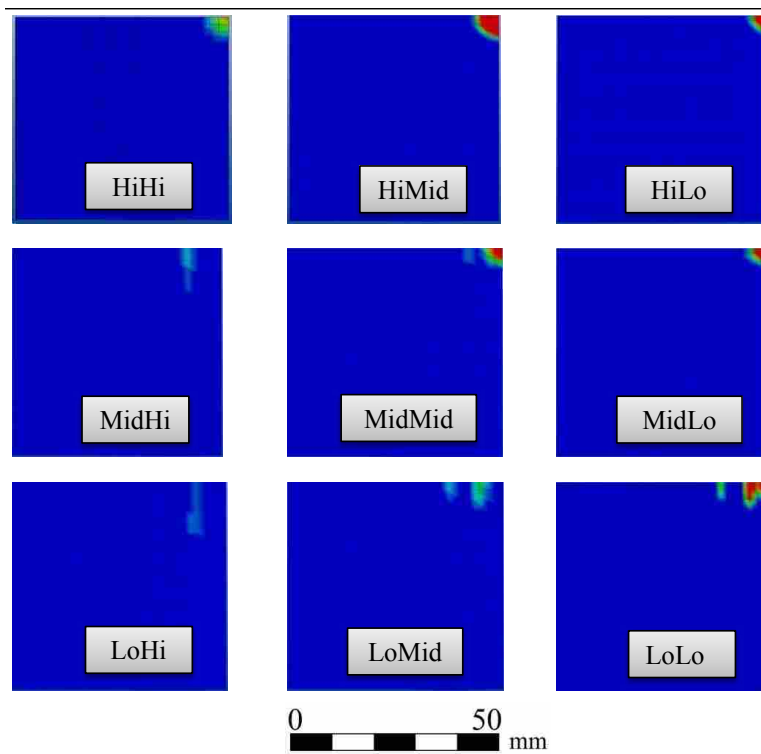
Figure 2.7: Contour plots of stress distribution in bottom surface elements based on dynamic 3D FEA.
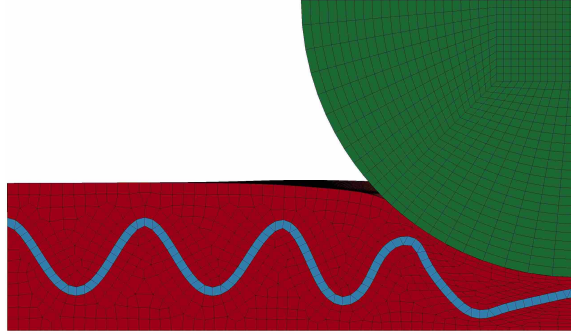
Figure 2.8: Finite Element prediction of the maximum deformation during impact to the MidMid configuration.
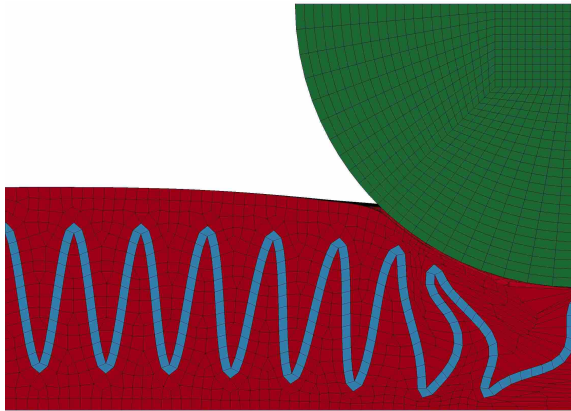
Figure 2.9: Finite Element prediction of the maximum deformation of LoHi configuration showing buckling of corrugation.

buckling mode of deformation, as shown in Figure 2.9. These two shapes also had the lowest peak accelerations.

2.3.3 Physical Drop Tests

The results from the drop tests are summarized in Table 2.2. The force width, W, refers to the size of the mark recorded by the pressure film and gives an indication of the force distributed through the padding. According to experiments conducted by Desmoulin and Anderson [38], the pressure distributions measured would likely correlate to the size of a bruise an athlete might receive from an impact. The value reported is the average of the widest and narrowest dimensions of the marks for two tests.

To compare the samples, a performance metric is proposed that accounts for the size, mass and force-distributing effectiveness of the padding samples. The metric is related to the peak pressure, P, the area density, ρ_A, and the impacted volume of the sample. The area density of the padding sample is the sample mass divided by the area of the padding normal to the loading direction. The impacted volume takes into account the padding thickness and the force transferred through the padding represented by the force width, W. The impacted volume, V_I, is approximated by a cylindrical volume whose diameter is the force width, W, and whose length is the sample thickness, t, as

$$V_I = \frac{\pi}{4} W^2 t \tag{2.1}$$

For the purpose of a metric for comparing samples, the constant, $\pi/4$, can be neglected. The performance metric, M_P, is then

$$M_P = \rho_A P t W^2 \tag{2.2}$$

The metric is made dimensionless by dividing the M_P value of each sample by that of the foam-only sample as

$$M_R = \frac{(M_P)_{sample}}{(M_P)_{foam}} \tag{2.3}$$

Table 2.2: Results from drop tests.

Corrugation	Mass (g)	Sample Thickness Total (t) / Corrugate (mm)	Force Width, W (mm)	Peak Pressure, P (MPa)	Performance Metric, M_R
LoLo	34.8	9.9 / 3.4	17.6	45	0.47
LoMid	43.7	12.4 / 5.4	25.6	25	1.09
MidMid	37.7	12.1 / 4.6	17.8	47	0.81
Foam only	31.3	12.7	19.1	55	1.00

14
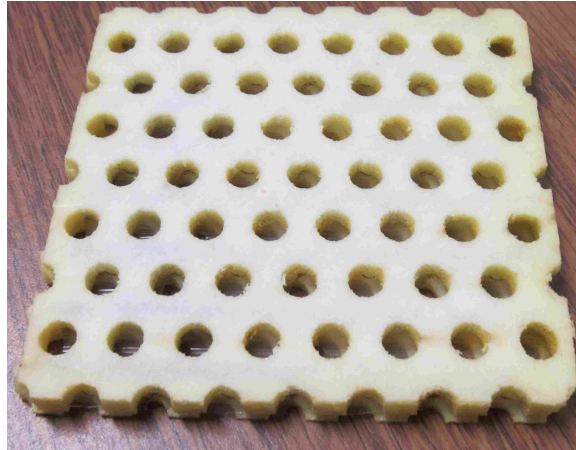
Figure 2.10: Example of holes cut in perforated samples.

A value of $M_R < 1$ would mean the corrugated sample has a combined mass, peak pressure and volume lower than foam alone which would indicate a more effective padding.

All three corrugation samples transferred lower peak pressures than the foam alone. Of the three corrugated samples, the LoMid configuration transferred the lowest amount of pressure to the pressure film, and the MidMid configuration transferred the highest. By comparing the M_R values, we can see that although the LoMid configuration transferred the lowest peak pressure, its volume and mass put it at a disadvantage to the LoLo sample which is a more effective padding in terms of mass and volume compared to foam alone. The MidMid sample also has a M_R value of less than one indicating it is also more effective than foam alone. Buckling was observed in the drop test onto the LoMid sample which resulted in permanent deformation in the polycarbonate.

For one set of samples, after initial drop testing, an array of holes was cut into the samples (see Figure 2.10) using a laser cutter and the samples were re-tested. The results of these before and after tests are shown in Table 2.3. It can be observed that perforating the samples reduced the weight by an average of 22% and increased the peak pressure by an average of 19%. It should be noted that laser cutting the holes may have affected the material properties of the polycarbonate due to the high heat of the laser. In all the laser perforated samples, some permanent deformation occurred.

The results of the drop tests were also compared to the dynamic FEA. Figure 2.11 shows the similarity of the pressure distribution for the MidMid and the LoMid configurations. While the overall pressure patterns of the results are similar, the FEA underestimated the peak pressure
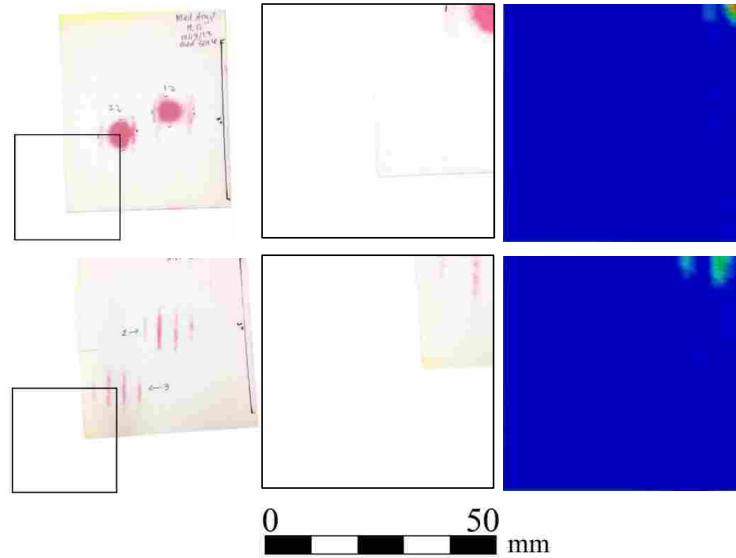
Figure 2.11: Comparison of drop test and FEA pressure distributions, Top: MidMid, Bottom: LoMid.

by a percent difference of about 30%. This difference may be due to effects associated with material nonlinearity in the foam constitutive behavior as well as geometric nonlinearities due to the interfacial conditions between the foam and the corrugate [39]. Also, the FEA did not account for material failure or damage. In addition, the use of pressure sensitive film to record peak pressure may account for some inaccuracy due to variation and subjectivity in the manual color-to-pressure mapping.

Table 2.3: Comparison of padding samples before and after perforation.

Corrugation	Weight (g)			Peak Pressure (MPa)			Force Width (mm)		
	Before	After	Change	Before	After	%Change	Before	After	%Change
LoLo	21.5	16.75	- 22%	65	75	+ 15%	25	34	+ 36%
LoMid	27.5	22.54	- 18%	45	65	+ 40%	18	17	- 5%
MidMid	26.34	19.45	- 26%	65	65	0%	24	17	- 30%

2.4 Discussion

A key to the corrugated padding concept is not just the use of a corrugation to stiffen the padding, but also to enable elastic deflection of the corrugation to absorb energy from impacts. The first factor to consider in designing a corrugation is the basic shape of the corrugated wave. Four shapes were tested in this study using a configuration of equal peak-to-peak height and length. The wave shape of the corrugation did not significantly alter the force of deflection. This result would tend to indicate that many wave shapes could be used in a corrugation to achieve equivalent energy absorption through compliance or elastic deflection.

However, this applies to the compliance along the corrugation only. The bending of the corrugation perpendicular to the cross section would also affect the overall elastic strain energy stored in the corrugation. Bending stiffness in this direction would be dependent on the area moment of inertia (MOI) of the corrugation cross section in which case the arc wave (Figure 2.2) would have the highest MOI and the triangle wave would have the lowest.

For a given corrugation wave shape, the properties of the wave (its wavelength and amplitude) will also affect its ability to absorb energy. From the quasi-static analyses, we learn that the energy absorbed per unit mass tends to be greatest for corrugations with a longer wavelength and higher amplitude. The dynamic analysis results show the configurations with a desirable acceleration pulse tended to be the ones with a higher amplitude wave. The peaks of the acceleration pulses for each configuration tended to be grouped in time according to the amplitude level. At each level, the lowest peak acceleration was experienced by the corrugation where the wavelength and amplitude were equal (ie. HiHi, MidMid, and LoLo.) In both analyses, the HiHi configuration had the best performance.

The data suggest that for a given application, the goal would be to maximize the wave height within the design constraints, and then choose a wavelength such that the peak-to-peak height and length are equal. The performance metric developed (Equation [2]) provides a useful method for comparing basic data from impact tests. The metric takes into account the parameters of padding samples that are most important to its performance in sporting applications. Specifically, the impacted area can be thought of as relating to the size of a bruise that an athlete might develop as the result of an impact. Also, minimizing the thickness and mass of athletic padding is important to athletes and affects their decision on whether or not to use certain types of padding.

17

The data required to implement this metric can be collected through simple tests requiring little to no specialized instrumentation. The metric can be employed to compare samples to a control design, such as a foam only sample.

According to the performance metric presented in this study, the LoLo sample was the most effective padding sample compared to foam alone. This means that for a given weight and padding thickness, the LoLo corrugated padding prototype will provide better protection from impact forces than foam alone. Stated another way, to achieve the same amount of impact protection, a foam only sample would need to be much thicker. Also, while the LoMid sample transferred the lowest peak pressure, it was at a cost of being significantly heavier than the other samples tested.

The subsequent perforation and retesting of some of the corrugated padding prototypes provided an exploration of a method to further reduce the weight of the corrugated padding concept since weight is often a critical property for many sports applications. Perforation appears to be an effective method of reducing the weight; however, there is some reduction in the ability of the padding to distribute the impact forces. Generally, after perforation, the peak pressure increased while the area of the force distribution decreased. Also, the cutting process with a laser may have affected the mechanical properties of the polycarbonate corrugation. This effect was specific to this prototyping process and could be reduced or eliminated through other manufacturing processes more conducive to larger scale production.

The FEA predicted that low wavelength, high amplitude corrugation configurations would experience buckling under load. This was verified with physical testing, which also showed that the buckling often resulted in some permanent deformation of the corrugated material. Permanent deformation may not be desirable for some padding applications where the padding must withstand multiple impacts. In which case, as mentioned the best configuration would be to match the peak-to-peak length and height. However, plastic deformation may be suited for other applications, such as bike helmets. In those cases, a short wavelength and high amplitude corrugation can be effective at dissipating energy and distributing impact forces.

2.5   Conclusions

This study investigated the important parameters for energy absorption and force distribution of an innovative padding concept. The concept has potential for use in sports applications

to protect athletes from certain injuries. Through FEA and physical testing, it was found that the wave shape of the corrugation may not be a major factor in the energy absorption. The best performance of the corrugate for elastic energy absorption is achieved when the wave has peak-to-peak height and length that are equal. For one-use types of applications, more energy absorption can be achieved with configurations with a high amplitude and lower wavelength. These configurations tend to produce buckling and plastic deformation and may not be reusable. The weight of the padding may be reduced by perforating the foam and corrugation, however this may increase the peak forces transferred through the padding.

A key advantage of this padding concept comes through the mechanical behavior of the corrugate. A corrugation increases the bending stiffness of a sheet about the axis parallel to the cross-section of the corrugate while maintaining a lower bending stiffness about an axis perpendicular to the cross-section. This idea may be exploited to produce padding specific to a certain body part and motion. Other corrugation shapes may also prove beneficial for certain motions or applications. For example, rather than a straight corrugation, curved or orthogonal corrugations may also be beneficial. A particular corrugation with a configuration of two mutually orthogonal corrugations has its roots in origami [40]. This particular fold pattern, the Miura-ori [41], exhibits unique mechanical properties which may also be beneficial when used in an energy absorbing application such as this padding concept.

This work has introduced and explored an innovative padding concept that may be useful to meet the needs of athletes to provide a light, effective padding that protects them from impact injuries and does not interfere with their ability to compete in their sport. Further work will explore the properties of other corrugations, specifically origami-inspired corrugations, for their usefulness in elastic energy absorption applications. Also, other materials and manufacturing processes may be investigated that would produce lighter designs while still providing a desired level of protection.

CHAPTER 3.   ELASTIC ENERGY ABSORPTION OF ORIGAMI-BASED CORRUGA-
TIONS

3.1   Introduction

A common engineering challenge is the design of systems to absorb kinetic energy and distribute applied forces through reusable means. Some examples of applications where reuse is important include athletic padding and helmets, protective shipping materials, mats and playground coverings. In such applications, elastic energy absorption is necessary since energy is absorbed through a temporary deformation of the material which is subsequently restored allowing for multiple deflections. Innovations that provide new methods for absorbing energy elastically would be valuable to engineers facing such design challenges. Recent work in the application of techniques, theories and principles learned from the study of origami may inspire innovative designs with the potential of solving such practical engineering problems.

A specific class of origami design focuses on creating folding patterns which result in either two- or three-dimensional geometric tessellations. One such tessellation is called the Miura-ori. The pattern is shown in Figure 3.1. This particular tessellation has received much attention in the engineering literature because of its simplicity and intriguing mechanical properties. The folding pattern takes its name from Koryo Miura who first proposed it in the early 1970s. Miura [41] presented the fold as part of a sandwich-core he called "Zeta-Core," where the core is a corrugate resulting from superposing two corrugations in mutually orthogonal directions. Klett and Drechsler [42] described this pattern as a double developable corrugation while Lebee and Sab [43] investigated the use of this "chevron pattern" in foldcore materials. Miura [44] later found that a variation of the principal design of this double corrugation could be used for folding and deploying large membranes for space applications. The Miura-ori was also found by Kobayashi [45] to be naturally occurring in hornbeam and beech tree leaves. The auxetic characteristic of the fold

Figure 3.1: Example of Miura-ori tessellation folded in paper.

pattern (it has a planar expansion in two orthogonal directions) can be observed in the unfolding of leaves from these two types of trees.

The geometry of the Miura-ori fold pattern has been well defined in the literature. Tachi [46] studied its geometry and developed a general model for a rigid foldable quadrilateral mesh. Stachel [47–49] also studied the geometry of the Miura-ori as well as a more general quadrilateral mesh and defined the conditions which allow it to be continuously flexible. Shenk and Guest [50] describe the intriguing auxetic property of the Miura-ori tessellation (it has a negative Poissons ratio for in-plane stretching) but yet deforms anticlastically (into a saddle shape) under out-of-plane bending. To describe the bending stiffness of the Miura-ori tessellations, Schenk and Guest [51] applied a structural engineering approach where the tessellation was modeled as a pin-jointed bar framework. They applied a bending stiffness to describe both bending of the facets and the bending along the fold line. Shenk and Guest [52] also proposed two configurations of the Miura-ori fold to create metamaterials that may have several practical applications. Gattas et al. [53] also studied the geometry of the Miura-ori tessellation and derivative patterns developed by altering one characteristic of the Miura pattern. Tolman et al. [54] investigated various wave patterns of compliant corrugations as possible means of elastically absorbing energy for athletic padding applications.

The unique kinematic properties of the Miura-ori are of special interest. When employed dynamically, the Miura-ori can be considered a compliant mechanism since its motion is derived from the deflection of the material at its folds. As such, the mechanism can be studied using a

21

Pseudo-Rigid-Body Model (PRBM) [1] in which the facets are considered links and the folds are considered hinges or pin joints with the pin axes aligned with the folds [40]. Greenberg et al. [55] demonstrated the approach of modeling kinetic origami using the PRBM.

By closely examining a single unit cell of the Miura-ori tessellation (Figrue 3.2), one can observe that each fold intersects at a single point. Since the folds act as pin joints whose axes are directed along the fold line, each unit cell of the tessellation is a four-bar spherical mechanism. This basic type of spherical mechanism has been thoroughly studied and its kinematics defined by several researchers [56–58].

This study focuses on the potential of the Miura-ori to be used in elastic energy absorbing applications. The energy absorbing characteristics of the Miura-ori tessellation and other origami-inspired designs have been studied by other researchers, however, their research has focused on plastic deformation from impact loading or crushing of the folded material. Ma and You [59–61] and Gattas and You [62] studied energy absorption through plastic deformation of several origami-inspired shapes including a modified Miura pattern referred to as an "indented foldcore". Basily and Elsayed [63] looked specifically at the energy absorption characteristics of what they called "folded chevron patterns." These patterns were similar to Miura-ori created using metal sheets and then loaded dynamically. The energy absorption mode was plastic deformation of the material. Audoly and Boudaoud [64] modeled the buckling behavior of a thin elastic plate bonded to a compliant substrate. In this case they found that the Miura-ori pattern served well as a geometric model for a herringbone buckling mode observed in experiments. Heimbs [65, 66] studied the impact strength and behavior of "foldcore sandwich structures," which consisted of a Miura-ori corrugation sandwiched between two plates. Particularly, Heimbs studied the application of composites in creating the foldcore.

In this study, the elastic energy absorbing characteristics of the Miura-ori unit cell is investigated. Since the tessellated pattern expands auxetically in plane when strained, it is hypothesized that this behavior may be advantageous for absorbing energy as it would allow for the distribution of elastic strain across the tessellation. To better understand this behavior and its relationship to energy absorption, a pseudo-rigid-body kinematic model is developed. The kinematic model is then combined with a virtual work analysis to derive a kinetic model of a single unit cell of the tessellation. The analytical models are verified through comparison with data in the literature for

similar models and also using a commercial 3D simulation software. These analytical models are used to explore how the main geometrical parameters affect the force and energy absorption properties of the Miura-ori. Testing of physical prototypes is used to determine the best parameters for the model. This approach may be applied to similar origami tessellations and may be beneficial for the design of innovative devices for elastic energy absorption applications.

3.2   Method

3.2.1   Kinematic Model

The Miura-ori tessellation is composed of a pattern of repeating parallelograms that can be defined by the length of their adjacent sides, a and b, and their acute interior angles α as shown in Figure 3.2. To describe the kinematics of a single unit cell, the notation defined by Lang [58] is adopted as shown in Figure 3.3. Here α_1 through α_4 are the sector angles or the in-plane angles between the fold lines. The dihedral angles, γ_1 through γ_4, describe the deviation from straightness of the folded faces with $\gamma = 0$ corresponding to a flat sheet and $\gamma = \pi$ describing the fully folded state. The angles between the planes are denoted as β where $\beta = \pi - \gamma$. For the Miura-ori, $\gamma_1 = \gamma_3$ and $\gamma_2 = \gamma_4$. By examining the unit cell inside a unit sphere, and analysing it as a spherical mechanism, the spherical links have a length of $\alpha_1 - \alpha_4$. As derived by Lang [58], the angle between the two fold lines which lie along the plane of symmetry for the unit cell, ζ, is given by

$$\cos \zeta = \cos \alpha_1 \cos \alpha_2 + \sin \alpha_1 \sin \alpha_2 \cos(\pi - \gamma_2) \tag{3.1}$$

This equation can be rearranged to give the value of dihedral angle γ_2 given the sector angles α_1 and α_2.

$$\gamma_2 = \pi - \cos^{-1} \left(\frac{\cos \zeta - \cos \alpha_1 \cos \alpha_2}{\sin \alpha_1 \sin \alpha_2} \right) \tag{3.2}$$

Lang [58] further derived the relationship between adjacent dihedral angles as

$$\gamma_1 = \cos^{-1} \left(\frac{\sin \alpha_1 \sin \alpha_2 \sin^2 \gamma_2}{1 - \cos \zeta} \right) \tag{3.3}$$

23
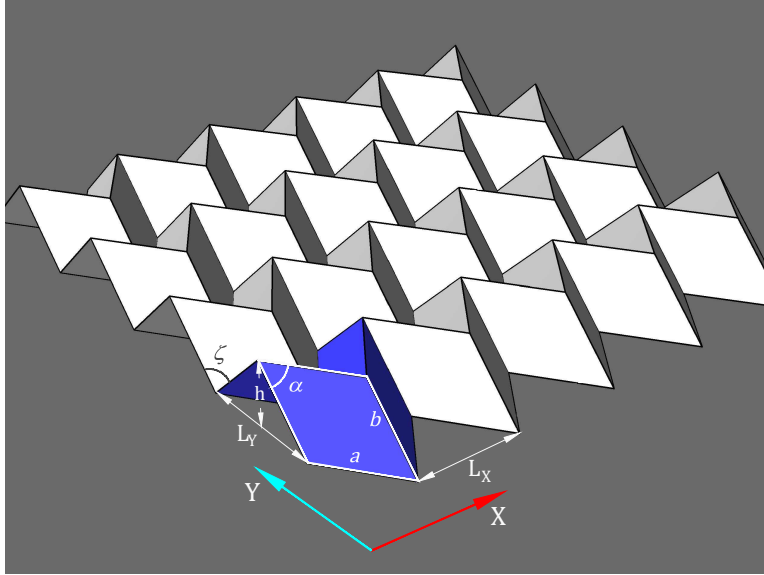
Figure 3.2: Miura-ori unit cell parameters and principal strain directions, X and Y.
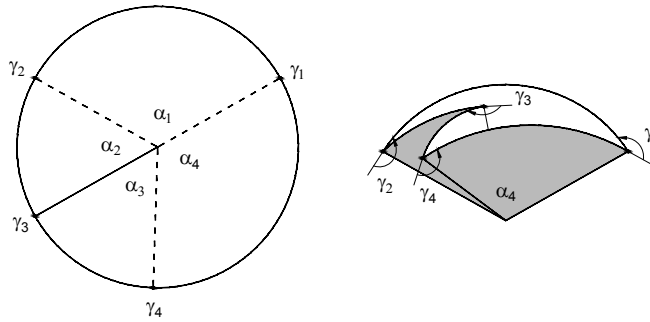
Figure 3.3: Spherical geometry notation as presented by Lang [58] of a unit cell cropped by a unit circle shown flat on the left and folded on the right.

Using these relationships developed by Lang for the three-dimensional angles of a degree-4 vertex, we will apply the geometry of the Miura-ori unit cell to arrive at the kinematic relationships. The principal directions of strain for the Miura-ori are shown as the two orthogonal axes, X and Y, in Figure 3.2. For a unit cell, length L_Y is defined in the direction of the Y axis as

$$L_Y = 2a\sin\left(\frac{\zeta}{2}\right) \qquad (3.4)$$
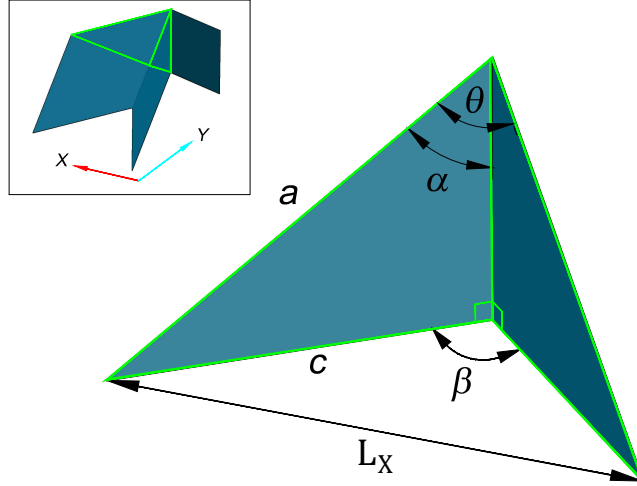
Figure 3.4: Description of paramaters used to derive θ and L_X.

In the X direction, length L_X is found by defining an angle, θ, as shown in Figure 3.4. The green lines indicate how the larger figure fits inside a unit cell. The angle θ can be related to the angles α and β by applying the Law of Cosines to the two triangles formed by adjacent sides to these angles b and c (where $c = b\sin\alpha$). Both of these triangles share the common side, L_X. Therefore,

$$\cos\theta = 1 - \sin^2\alpha\,(1 - \cos\beta) \tag{3.5}$$

and

$$L_X = 2b\sin\left(\frac{\theta}{2}\right) \tag{3.6}$$

3.2.2 Kinetic Model from Virtual Work

A virtual work analysis [1] is developed for two different models of the Miura-ori unit cell where the facets are assumed to be rigid. The first model assumes the storage of elastic strain energy to be in the folds or hinges of the Miura-ori unit cell. This will be referred to as the *hinge* model. Through the application of the PRBM (Figure 3.5a), the strain energy is modeled as the deflection of torsional springs with linear stiffness values of k_{T1} and k_{T2}. A second model is developed for a concept in which the Miura-ori is used to achieve an in-plane auxetic expansion

25

(a) Hinge PRBM   (b) Membrane PRBM
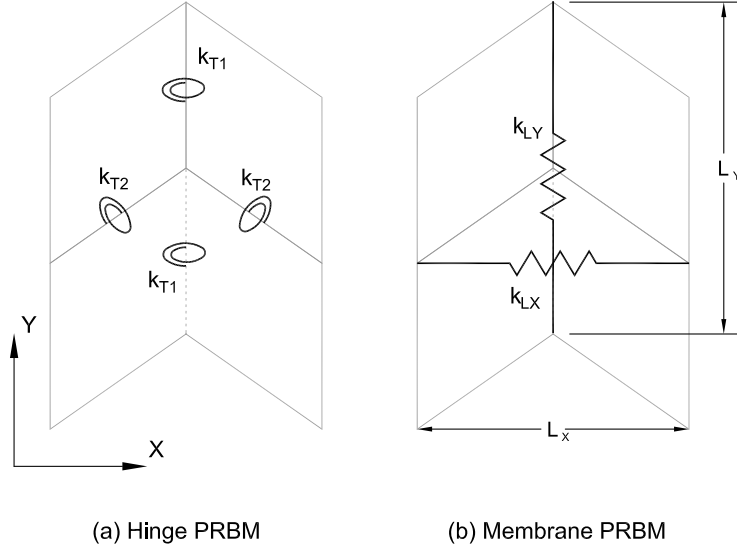
Figure 3.5: PRBM of the hinge and membrane concepts.

of an attached elastic membrane. This will be referred to as the *membrane* model (Figure 3.5b). It is assumed that the elastic strain energy of the membrane can be represented by two linear springs attached to the bottom vertices of the unit cell such that they are aligned with the two primary directions of motion. The linear spring constants in this model are k_{LX} and k_{LY}. A coordinate system was chosen such that the origin is on the surface on which the unit cell rests with the z-axis being vertically upward and passing through the central vertex. The distance of the vertex from the origin or the surface is defined as h (shown in Figure 3.2) and can be defined as a function of ζ as

$$h = b\cos\frac{\zeta}{2} \tag{3.7}$$

Additionally, several variables related to h are defined that will be useful in the discussion of the data from these models and the prototype testing. If the tessellation is fully compressed in the X-direction, the maximum height of the central vertex, H, is defined as

$$H = b\sin\alpha \tag{3.8}$$

The height of the vertex in its starting, undeflected position is defined as h_0 and the displacement of the vertex, δ is

$$\delta = h_0 - h \tag{3.9}$$

Further, two non-dimensional parameters of height are defined as %h and %H where

$$\%h = h/h_0 * 100 \tag{3.10}$$

and

$$\%H = h/H * 100 \tag{3.11}$$

The virtual work analysis applied to each model results in an equation that describes the force-deflection characteristic of the unit cell in the z-direction for each model. The analysis was done with respect to the generalized coordinate, ζ. The virtual work, δW, associated with an applied load in the z-direction is

$$\delta W = -F \frac{dh}{d\zeta} \delta \zeta \tag{3.12}$$

The potential energy developed from the deflection of each hinge, i, of the hinge model is

$$V_i = k_{Ti}(\gamma_i - \gamma_{i0}) \tag{3.13}$$

and for each linear spring, j, of the membrane model is

$$V_j = k_{Lj}(L_j - L_{j0}) \tag{3.14}$$

The total virtual work is the sum of the work due to the input virtual displacement, $\delta \zeta$, of the input force (Equation 3.12) and the work from the potential energy of the virtual spring displacements found by differentiating Equations 3.13 and 3.14 with respect to ζ and multiplying by $\delta \zeta$. Applying the principle of virtual work [67] by setting δW equal to zero and dividing by $\delta \zeta$ yields an expression for the input force required to deflect the unit cell a distance of δ (Eq. 3.9). For the hinge model, F_H is

$$F_H = \left(\frac{dh}{d\zeta}\right)^{-1} \left[-2k_{T1}(\gamma_1 - \gamma_{1_0})\frac{d\gamma_1}{d\zeta} - 2k_{T2}(\gamma_2 - \gamma_{2_0})\frac{d\gamma_2}{d\zeta}\right] \tag{3.15}$$

where the terms $\frac{d\gamma_2}{d\zeta}$, $\frac{d\gamma_1}{d\zeta}$, and $\frac{dh}{d\zeta}$ are kinematic coefficients found by differentiating Eqs. (3.2, 3.3 and 3.7) with respect to ζ and are defined as

$$\frac{d\gamma_2}{d\zeta} = -\sin(\zeta)\left[(\sin\alpha_1 \sin\alpha_2)\sqrt{1 - \left(\frac{\cos\zeta - \cos\alpha_1 \cos\alpha_2}{\sin\alpha_1 \sin\alpha_2}\right)^2}\right]^{-1} \tag{3.16}$$

$$\frac{d\gamma_1}{d\zeta} = \frac{-1}{\sqrt{1 - \cos^2\gamma_1}}\left[-\sin\gamma_2\frac{d\gamma_2}{d\zeta} + \frac{\sin\alpha_1 \sin\alpha_2 \sin(2\gamma_2)}{1 - \cos\zeta}\frac{d\gamma_2}{d\zeta}\right.$$
$$\left. - \frac{\sin\alpha_1 \sin\alpha_2 \sin^2\gamma_2 \sin\zeta}{(1 - \cos\zeta)^2}\right] \tag{3.17}$$

$$\frac{dh}{d\zeta} = -\frac{b}{2}\sin\left(\frac{\zeta}{2}\right) \tag{3.18}$$

The input force required to deflect the membrane model, F_M, a distance of δ (Eq. 3.9) is

$$F_M = \left(\frac{dh}{d\zeta}\right)^{-1}\left[-k_{L1}(L_Y - L_{Y0})\frac{dL_Y}{d\zeta} - k_{L2}(L_X - L_{X0})\frac{dL_X}{d\zeta}\right] \tag{3.19}$$

where the terms $\frac{dL_Y}{d\zeta}$ and $\frac{dL_X}{d\zeta}$ are kinematic coefficients found by differentiating Eqs. (3.4) and (3.6) with respect to ζ and are defined as

$$\frac{dL_Y}{d\zeta} = b\cos\left(\frac{\zeta}{2}\right) \tag{3.20}$$

28

$$\frac{dL_X}{d\zeta} = a\cos\left(\frac{\theta}{2}\right)\frac{d\theta}{d\zeta} \tag{3.21}$$

Eq. (3.21) also includes the term $\dfrac{d\theta}{d\zeta}$, which is the derivative of Eq. (3.5) with respect to ζ, or

$$\frac{d\theta}{d\zeta} = \frac{-1}{\sqrt{1-\cos^2\theta}}\left[sin^2\alpha_1\sin\beta_1\frac{d\gamma_1}{d\zeta} + (1-cos\beta_1)\right] \tag{3.22}$$

3.2.3   3D Simulation

To verify the analytical kinetic hinge model of the Miura-ori unit cell, a 3D simulation was done using the Solidworks software. An assembly was constructed using planar surfaces that were constrained to meet at the edges to simulate the fold lines. The surfaces were assumed to be rigid. Torsional springs were placed along the fold lines with linear spring coefficients equal to those in the virtual work model. The program was then used to simulate the force-deflection properties of the assembly and compared to the predictions of the analytical model.

3.2.4   Physical Testing

Physical hardware was built and tested for both the hinge and membrane energy absorption concepts (Figure 3.6). The facets of the Miura-ori unit cell for both models were made of 3 mm thick acrylic so as to be stiff compared to the hinges.

Origami tessellations in paperboard material have complex mechanical behavior [68–70]. In this study the hinges were made from 0.4 mm nylon that was thermoformed to the appropriate starting angle and mechanically attached to the acrylic facets. To achieve a good approximation of a spherical mechanism the hardware was built with elastic hinges on the three joints representing the mountain folds of the Miura-ori unit cell. This allowed the axes of rotation of the hinges to intersect at a single point without the need to account for the thickness of the facets.

(a) Hinge test hardware   (b) Membrane test hardware
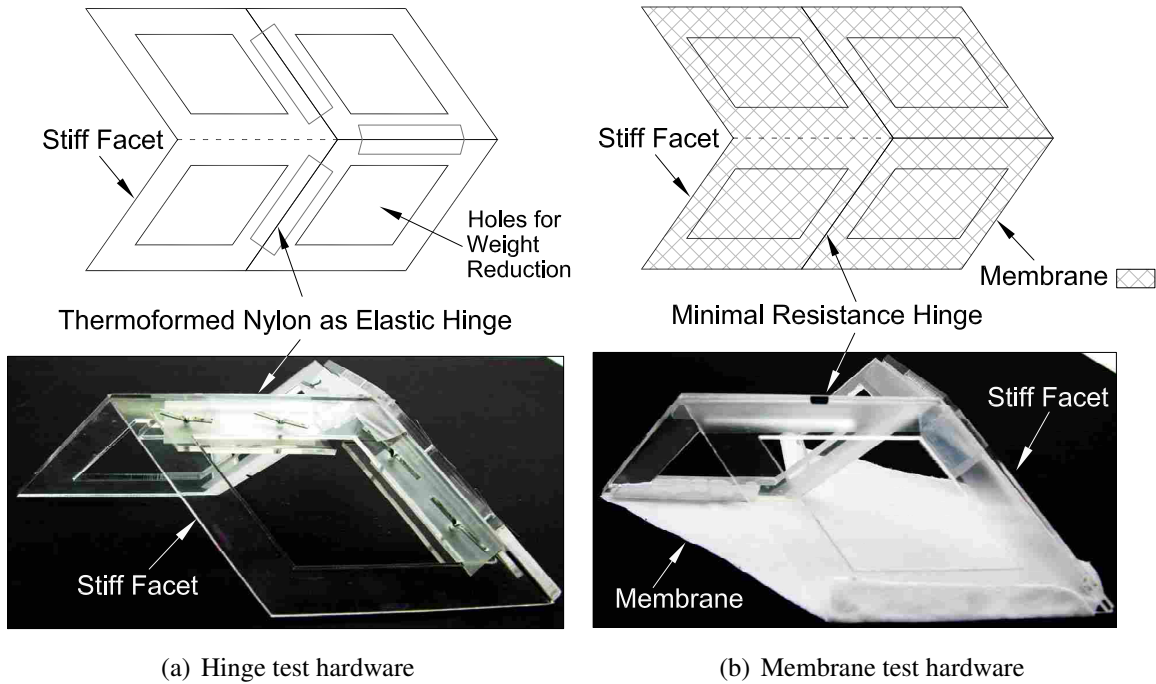
Figure 3.6: Physical test devices of Miura-ori unit cells for two methods of energy absorption.

The membrane hardware was assembled using thin adhesive tape to join the facets to minimize friction and strain energy absorbed at the hinges. A nylon and spandex fabric membrane was attached to the bottom of the unit cell.

To reduce the effect of friction from the expansion of the unit cell, the testing was done on a flat, smooth, polyethylene surface. Each model was quasi-statically loaded in the z-direction (vertically) using an Instron 3342 (0.5 kN capacity) universal testing machine with a 50 N load cell. The test setup is shown in Figure 3.7. The force-deflection characteristics of each prototype were measured and recorded.

The analytical models were used to determine the stiffness parameters of the hinges and the membrane. The stiffness coefficients were optimized to reduce the sum of the square of the residual between the model and the test data. This is of particular interest for the case of the membrane model to evaluate how well the two-orthogonal-spring assumption can represent an elastic membrane.
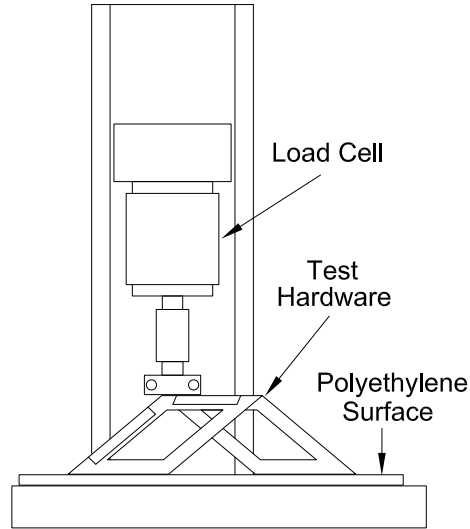
Figure 3.7: Test setup for measuring the force-deflection characteristics of the *hinge* and *membrane* unit cell prototypes.

3.3 Results & Discussion

3.3.1 Model Verification

Two methods were used to verify the analytical models: comparison with a Poisson ratio model from the literature, and 3D simulation using Solidworks. The Poisson's ratio for the unit cell, defined as the relative amount of expansion in its two principal directions, was calculated using the kinematic analytical model for the Miura-ori such that

$$\nu_{XY} = \frac{\varepsilon_Y}{\varepsilon_X} \tag{3.23}$$

where ε_X and ε_Y are the strains or changes in lengths L_X and L_Y. Figure 3.8 shows ν_{XY} as a function of $\%H$ for several different values of α. The results of Shenk and Guest [52], when translated to the same variables, result in a graph identical to Figure 3.8 which serves as one verification of the kinematic model. It can be seen that increasing α causes a greater expansion in the Y direction relative to the X.

The kinetic analytical model developed through virtual work analysis was compared to a 3D simulation done with Solidworks. Torsional spring stiffness were applied between the rigid facets of the modeled unit cell to calculate the force-deflection behavior. The same unit cell dimensions

31
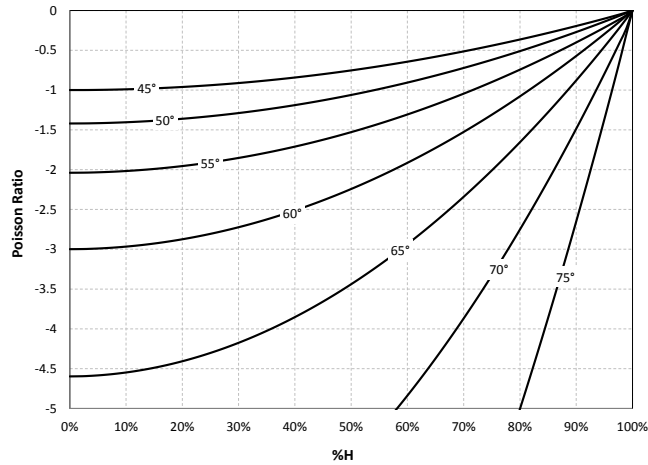
Figure 3.8: Poisson's ratios for several values of α as a function of the %H for a Miura-ori unit cell with $a/b = 1$.
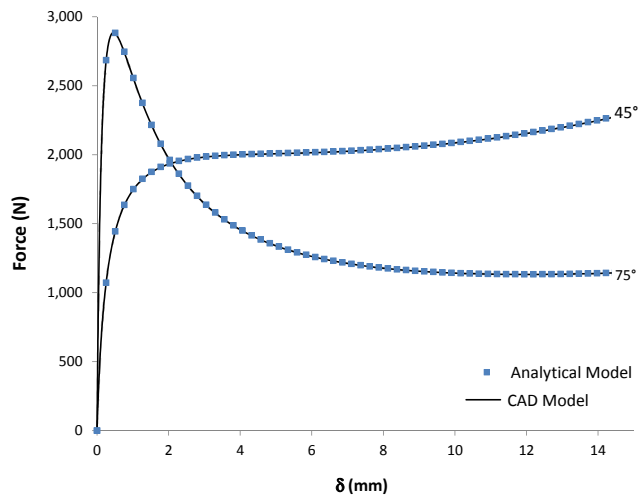
Figure 3.9: Comparison of force-deflection predictions for the CAD model and the analytical model

and spring stiffnesses were used in the analytical model and the Solidworks model. Figure 3.9 compares the predicted force-deflection curves for two variations of the geometry of the Miura-ori unit cell, where $\alpha = 45°$ and $\alpha = 75°$ ($a/b = 1$ for both), showing nearly identical results.

(a) Hinge model(stiffness in $N - mm/rad$)

(b) Membrane model (stiffness in N/mm)
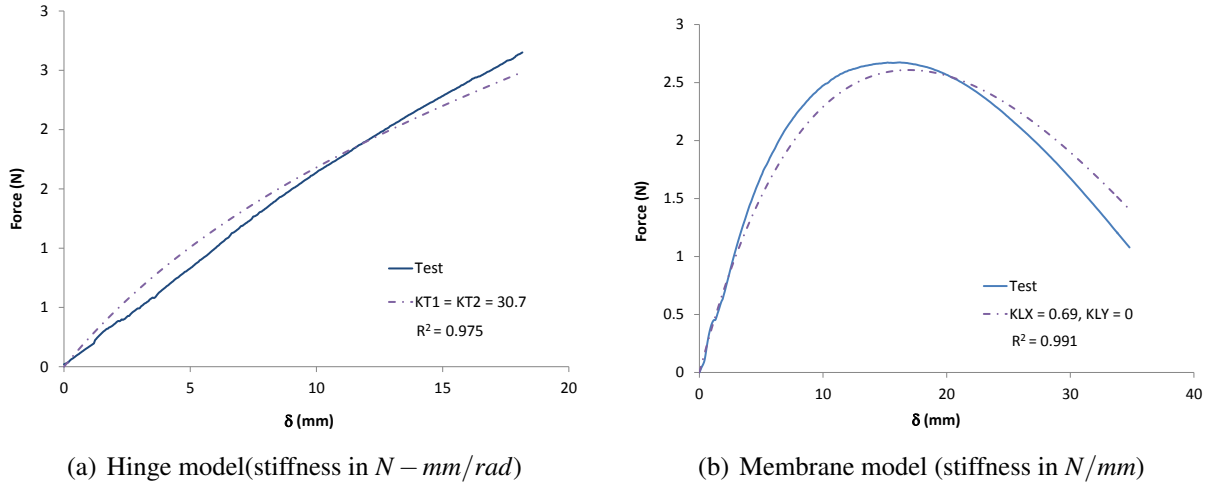
Figure 3.10: Force-deflection data from prototype tests compared to fitted curve based on analytical models.

3.3.2 Prototype Testing

Both the hinge and membrane analytical models were used to calibrate the model spring constants to generate force-deflection curves that best fit the quasi-static test data. The spring constants were optimized to minimize the square of the residuals between the test data and analytical models. The optimized fits are shown in Figure 3.10. In both cases, the analytical models were able to achieve a good fit of the test data.

Of particular interest was how well the membrane model fits the data from the physical prototype by representing the membrane using two linear orthogonal springs. As seen in Figure 3.10(b) a reasonable fit is achieved with k_{LX} being equal to zero. This is consistent with what is observed in the actual deflection of the membrane due to the expansion of the unit cell, where the main mode of strain across the membrane was primarily in the Y direction. For these values of α and a/b, it is reasonable to conclude that the force will be mainly determined by the strain in the Y direction and therefore using one spring stiffness can accurately represent the physical system tested. If a prototype were built with an array of unit cells across a tessellated sheet, the stiffness in the X direction would likely have a greater effect on the force-deflection curve.

3.3.3 Parameter Effects on Force

The verified kinetic models allow for the exploration of the effects of the geometrical parameters of the Miura-ori tessellation on the force-deflection and energy absorption characteristics of a unit cell. The parameters of interest (Figure 3.2) are the starting height of the unit cell's central vertex, h, the acute interior angle of the parallelogram, α, and the two adjacent side lengths of the parallelogram a and b .

The effects of the starting height of the central vertex, h, on the force-deflection curve can be seen in Figures 3.11 and 3.12. The maximum height of the central vertex for a given geometry is denoted H. The force-deflection curve is calculated for a given geometry at several initial heights, $\%H$. The force is plotted as a function of the percentage of the total deflection, $\%h$, of the central vertex.

For both the hinge and membrane models, a starting height greater than $90\%H$ results in a higher initial stiffness and peak force during the first 10% of the deflection. The general trend of the hinge model is to have a positive stiffness with the force generally increasing with deflection (except at a starting height of $99\%H$ where the force increases and then decreases before increasing again.) The membrane model has an initial positive stiffness but transitions to a negative stiffness with the force decreasing with deflection after reaching a peak force. For the hinge model, as the starting point decreases so does the stiffness, and it approaches a linear stiffness over the smaller deflection range. As the starting height of the membrane model decreases, the stiffness changes from positive to negative and approaches a near constant force over a small deflection range.

The force-deflection behavior for each configuration is determined largely by the mechanical advantage, or the ability of the unit cell to deform the elastic members (hinges or membrane) due to its geometry. At high starting points, the facets of the unit cell are nearly parallel to each other and to the line of action of the load applied to the central vertex. This results in a low mechanical advantage for straining the elastic hinges or membrane, thus requiring a higher applied load. As the unit cell expands, the mechanical advantage increases, which overcomes the increasing resisting forces due to the deflection of the elastic members. At lower starting heights, the change in the mechanical advantage is less extreme, which results in more consistent force-deflection behavior but over a smaller range of motion.
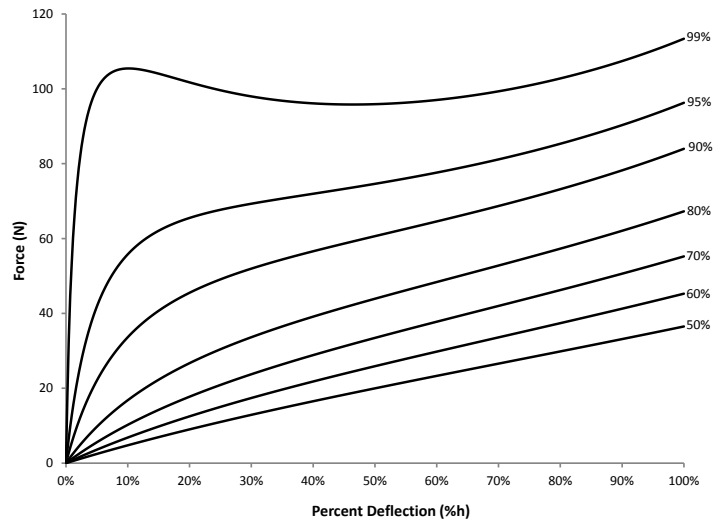
Figure 3.11: Force as a function of percent deflection for the hinge model at different vertex starting heights, $\%H$.
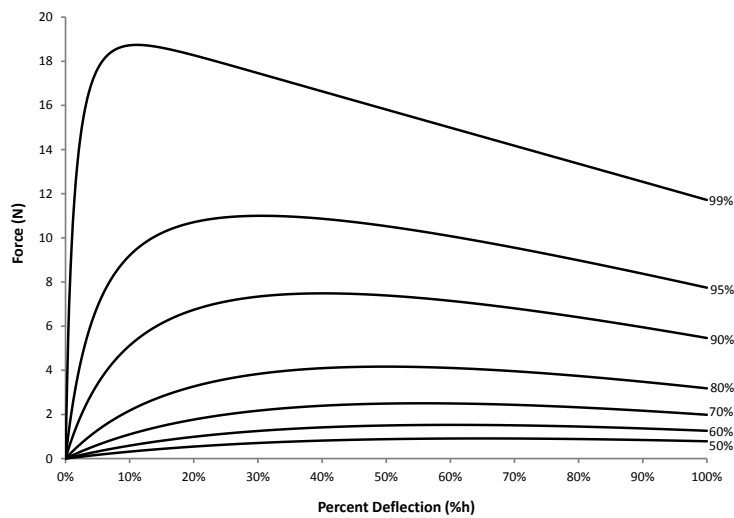
Figure 3.12: Force as a function of percent deflection for the membrane model at different vertex starting heights, $\%H$.

(a) Peak force   (b) Total energy
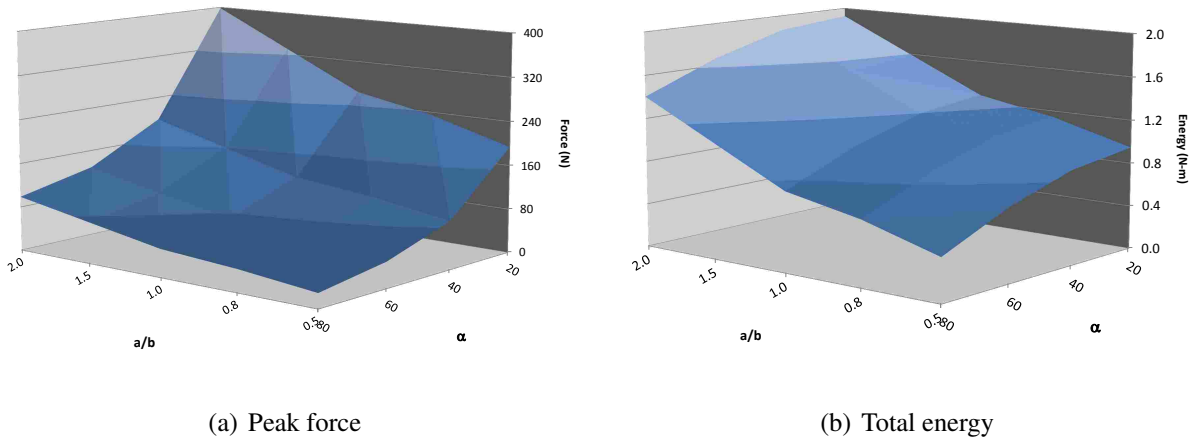
Figure 3.13: Surface plots for hinge model as a function of a/b and α.

Figures 3.13 and 3.14 show how the force-deflection and energy characteristics of the Miura-ori unit cell are affected by changes in a, b and α. The side lengths, a and b, are combined into one parameter by considering their ratio, a/b. The analytical models were used to calculate the peak force and the total work energy (area under the force-deflection curve) for hinge and membrane unit cells. Each configuration was calculated from a starting height of $\%H = 90$.

For the hinge unit cell, the peak force and the amount of energy absorbed increase with increasing a/b and decreasing α. For the membrane model, a/b appears to have a greater affect on both peak force and energy absorption at values of $a/b > 1$. It is interesting to observe that while the largest a/b and the smallest α resulted in the highest peak force, the highest total energy was absorbed at midrange values of α. Also at low values of a/b, both the peak force and total energy decreased with decreasing α though the difference over the range of α was small.

3.3.4 Total Tessellation Energy

The kinetic models for the hinge and membrane concepts allow for the calculation of the absorbed energy due to the deflection of a single unit cell. For a tessellation comprised of an array of unit cells, the total energy absorbed would be the sum of the strain energy from each cell. The total energy, E_T, would then be

(a) Peak force   (b) Total energy
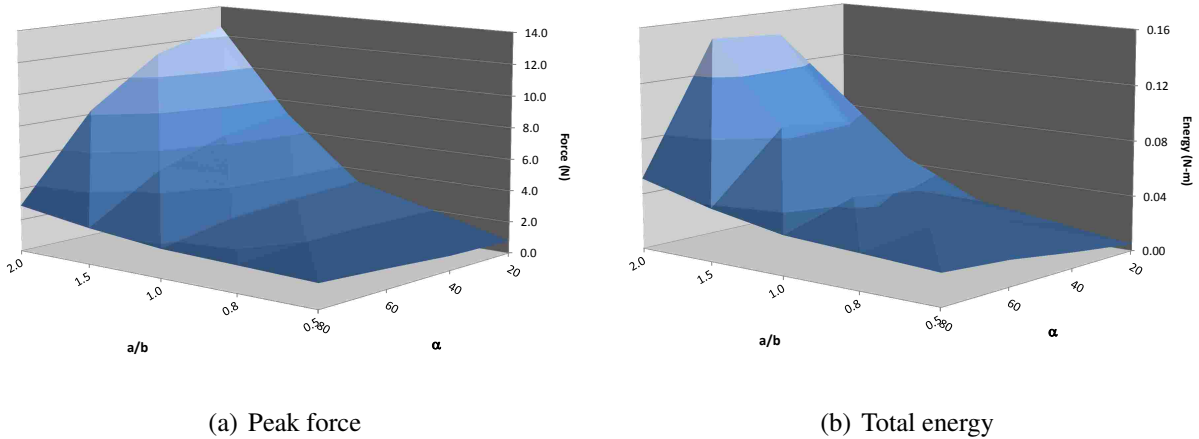
Figure 3.14: Surface plots for membrane model as a function of a/b and α.

$$E_T = E_u * N \tag{3.24}$$

where E_u is the energy for one unit cell and N is the number of unit cells in the array. The mode of energy absorption and the interconnection of the unit cells affects the method for summing the unit cells and is therefore different for the hinge and membrane models.

The membrane model is the simpler case. If the rows and columns are counted as shown in Figure 3.15 (assuming a full array with no half-cells), the number of cells is

$$N_m = R * C \tag{3.25}$$

where R is the total number of rows and C is the total number of columns of unit cells in the array.

For the hinge model, the total energy is accounted for by summing the unit cells that consist of four hinges meeting at a single vertex. Figure 3.15 shows how these unit cells mesh across the tessellation. The blue and green lines indicate opposite (i.e. mountain verses valley) central vertices. In the case of a square array where $R = C$, the total number of unit cells, N_h, is

$$N_h = 2R^2 - R + 1 \tag{3.26}$$
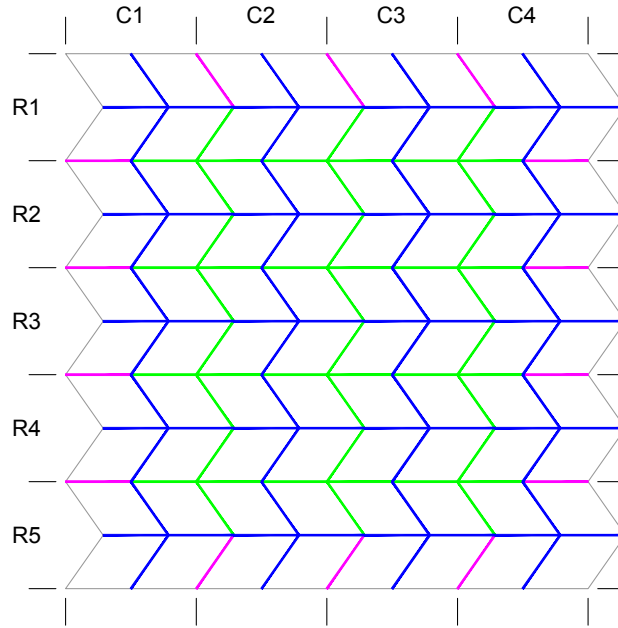
Figure 3.15: An array of Miura-ori unit cells with rows, R, and columns, C.

This equation accounts for the hinges around the edges of the tessellation (shown in magenta in Figure 3.15) which, in the case of a square array, can be summed to form a number of full, equivalent unit cells equal to the number of rows or columns of the array.

For a more general case where $R \neq C$, the edge (magenta) hinges cannot be equally divided into equivalent unit cells. The amount of strain energy in these *extra* hinges is dependent on the particular geometry, a, b, and α, as well as the starting height, $\%H$. It is therefore difficult to account exactly for the energy in these hinges. However, since each extra pair account for half of a unit cell, we will approximate their contribution in strain energy as being half of a unit cell's energy. It is convenient to orient the array so as to have more rows than columns as shown in Figure 3.15. With this orientation, the total number of unit cells, N_h, is

$$N_h \approx 2RC + \frac{1}{2}(R - 3C) + 1 \tag{3.27}$$

The majority of the energy absorbed by a hinged tessellation comes from the full unit cells. Therefore, the error in the total energy due to the approximation of the energy associated with the

extra hinges will be small. This error is further reduced if the tessellation is large and if R is close to C.

The preceding equations for total energy absorbed by a Miura-ori tessellation are based on an ideal model in which all of the deflection of the unit cells is in the hinges with no deflection in the faces or panels. They therefore represent a theoretical maximum distribution for the energy. A non-idealized tessellation would have some flexibility in the panels that would affect how the deflection is transferred across the tessellation. If a point load were applied to a single unit cell in a tessellated array, the deflection of the adjacent unit cells would decrease with the distance from the point of the applied load. The affect of the relative stiffnesses of the hinges and panels on energy absorption has been studied by Tolman et al. [54].

3.4 Conclusions

The analytical models developed in this study allowed for the investigation of how the geometrical parameters of the Miura-ori tessellation affect its elastic energy absorption properties. The starting height of the central vertex of the unit cell, *%H*, for both the hinge and membrane models affects the shape of the force-deflection curve. High starting values of *%H* above 90% create a large initial stiffness and high peak force due to decreased mechanical advantage in the unit cell. As the starting height decreases, so does the stiffness and the force-deflection curve tends to become more linear.

It was observed that both models of the Miura-ori tended to behave as nonlinear softening springs where the hinge model approached a linear response and the membrane model approached a constant force at low starting heights over a small deflection range.

The effects of the side lengths,(expressed as the ratio a/b), and the interior acute angle, α, of the tessellated parallelogram of the Miura-ori were also investigated. For both models, energy absorption and peak force tended to increase with increasing a/b and decreasing α with the exception that for the membrane model, more energy is absorbed in the midrange α between 40 and 60 degrees.

The total energy absorbed by a tessellation of unit cells can be approximated by multiplying the energy from a unit cell by the total number of cells in the array. The method of energy absorption affects how the unit cells are summed and is different for the hinge and membrane models.

The methods presented represent the theoretical maximum energy distribution based on idealized models.

This work lays a theoretical foundation for the use of the Miura-ori or similar origami tessellations in elastic energy absorption applications. The unique auxetic property of this and other origami folds have promise for elastic energy absorption applications because of their ability to distribute the strain across the tessellated pattern. Further work could be done to investigate how the models could be used to "tune" an energy absorption device based on the Miura-ori to achieve application-specific force-deflection curves. Also, these models could be used to study the effects of impacts to multiple unit cells. In addition, more exploration of materials and manufacturing processes to build mechanisms that achieve the desired motion while also absorbing energy will be necessary. For example, memory shape polymers may be advantageous for some applications [71]. Lastly, the affects of combining unit cells in different configurations such as though stacking may provide new insights into the mechanical properties and potential uses of these designs.

CHAPTER 4.   MATERIAL SELECTION FOR ELASTIC ENERGY ABSORPTION IN ORIGAMI-INSPIRED COMPLIANT CORRUGATIONS

4.1   Introduction

Many applications require designs that will absorb kinetic energy and distribute applied forces multiple times through reusable means. For example, preventing damage to equipment or products during transport or shipping requires that the packaging be able to withstand multiple drops or impacts. Also, people participating in contact sports often need protective equipment that can withstand multiple impacts, such as helmets and padding. In such cases, forces and energy are temporarily absorbed and redistributed through means of elastic deformation of some part of the protecting material. Common methods of elastic energy absorption include using foams, air-filled bladders or corrugated paper sandwich panels (cardboard).

Recently, much attention has been given to the potential for using origami in engineering applications. Origami-inspired designs have led to products that meet challenging design constraints. Such products include deployable solar arrays for satellite applications [72], medical stents [73], adaptive camouflage by means of morphing structures [74], car crash boxes with higher crumple zone energy dissipation [75], structural cores for aerospace applications which mitigate water retention in the sandwiched layers [42], airbag folding, and the 100 meter diameter Eyeglass Telescope [76].

A specific area of origami design focuses on creating folding patterns that result in either two- or three-dimensional geometric tessellations. A subset of these origami tessellations have the property of being *rigidly foldable* meaning that the geometry of the fold lines allow "continuous motion between folded states without the need for twisting or stretching of the facets between the creases" [46]. This subset of origami tessellations, when used as the basis for compliant mechanisms, show great promise for elastic energy absorption applications.
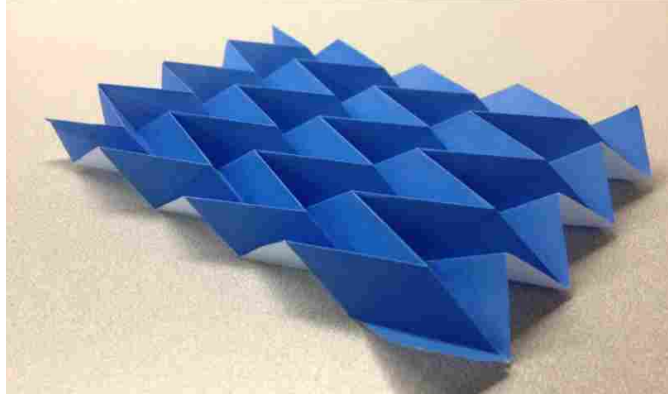
Figure 4.1: Example of Miura-ori tessellation folded in paper.

One such tessellation is the Miura-ori. An example, folded in paper, is shown in Figure 4.1. This particular tessellation has received much attention in the engineering literature because of its simplicity and intriguing mechanical properties. The folding pattern was first proposed by Miura [41] in the early 1970s as part of a sandwich-core where the core is a corrugate resulting from superposing two zig-zag corrugations in mutually orthogonal directions. The geometry and kinematics of the Miura-ori have been well defined by several researchers [46, 47, 49, 51]. Other researchers have investigated the ability of the Miura-ori to absorb and dissipate energy through crushing or plastically deforming the shape [63–66].

Due to its fold geometry, the Miura-ori is both rigidly foldable and auxetic for in-plane motion. That is, when stretched in one direction, the folded, tessellated, sheet simultaneously expands in the orthogonal, planar direction (having a negative Poisson's ratio) [77]. Additionally, a displacement applied normal to the plane of motion to a single vertex (fold intersection) of the tessellation, results in the planar, bi-directional expansion of the entire tessellation. Of course, the perfect distribution of the motion assumes rigid faces joined by perfect hinges. However, it is theorized that this unique property may be useful for absorbing energy elastically through the deformation of the folds and also distributing an applied force by redirecting it throughout the shape. Numerous applications stand to benefit from better understanding of the elastic energy absorption and force redistribution of this and other origami tessellations.

Compliant mechanism theory provides a bridge between traditional paper origami and origami-inspired designs using non-paper materials. Compliant mechanisms derive their motion

through the flexing of one or more of their members [67]. A crease or fold in paper can be considered to be a compliant member called a small-length flexural pivot [78]. By closely examining a single unit cell of the Miura-ori tessellation, one can observe that each fold intersects at a single point. Since the folds act as compliant hinges whose axes are directed along the fold lines, each unit cell of the tessellation is a compliant, four-bar, spherical mechanism. The mechanics of compliant mechanisms can be modeled using rigid members combined with torsional springs through the application of the *Pseudo-Rigid-Body-Model* approach [67].

To use origami tessellations like the Miura-ori for energy absorption and force distribution, it is important to identify and select non-paper materials with properties that are suited for these applications. The goal of elastic energy absorption is to transform kinetic energy into elastic strain energy through the deformation of an elastic material. Materials can be made to absorb energy more efficiently by changing the geometry [79] or method of manufacturing [80]. The material used in the tessellations must also be compliant to allow for the motion of the mechanism. The peak elastic strain of a linear elastic material is S_y/E where S_y is the yield stress and E is the elastic modulus of the material. Materials with higher S_y/E have been identified as more suitable candidates for compliant mechanisms [67]. Several methods have been identified for selecting materials for compliant mechanisms in specific applications [81–83]. In addition, for most energy absorbing applications, the mass or density and the cost of the material are important considerations. Ashby [2] has developed a method for material selection in mechanical design in which a material index is derived based on the relevant material properties and mechanical models for a given application. Graphical charts which display many materials according to these relevant material properties are then created and used to find the material which optimizes the material index.

This study investigates material-related issues pertaining to the design of origami-based compliant mechanisms for elastic energy absorption and force distribution. It presents the analysis and development of a method for material selection based on key material properties relating to the mechanical performance of these mechanisms. This method is a three-step process that begins with screening materials based on elastic strain and modulus values, which leads to the selection of a suitable subclass of material for compliant-mechanism-type applications, such as the Muira-Ori energy-absorbing cushion. Second, the Ashby method is used to provide an efficient means for refining the choice of material further by optimizing particular properties of the final component

(such as mass, cost, resilience) within the applied engineering constraints. Third, specific stiffness characteristics are chosen to deliver improved force distribution and energy absorption properties for a peak desired force transfer. These characteristics can be achieved through a combination of detailed geometry and/or local material choice and are investigated in this study through Finite Element Analysis (FEA). The development of this method will be important in the transition of origami-inspired design from paper to other materials [84]. While this work will focus specifically on the Miura-ori tessellation, the results will provide a valuable design tool that may be applied to similar patterns for elastic energy absorption and force distribution applications.

4.2 Method

When designing an origami-inspired, folded mechanism for energy absorption applications, there are three main material-related issues to consider. The first is to select a material that can allow the joints or hinges of the tessellation to deform elastically to achieve the desired motion while also providing enough stiffness in the tessellation panels to resist bending. A material that has a higher elastic strain (S_y/E) is a better candidate for compliant mechanisms. Also, a minimum elastic modulus should be identified for an application. Therefore, the first step of the material selection method for energy absorbing, compliant corrugations is to screen the materials based on their modulus and peak elastic strain.

The second issue is to select a material that will meet the requirements for the specific application (i.e. optimize the functionality of most importance, within the constraints of the engineering application). For the applications of interest in this work, it is desirable that the mechanism is able to deflect and store elastic strain energy, but also result in a final design that is light weight or cost-effective. The Ashby method of material selection can be applied to develop a material index that is specific to these parameters. This second step of the material selection method allows for identification of optimal materials for these mechanisms.

The third consideration is the stiffness of the folds, or compliant hinges, as compared to that of the tessellated faces and how this stiffness ratio affects the auxetic motion, force distribution and energy absorption of the mechanism. This is studied using FEA. Selecting a stiffness ratio for specific energy absorption and force distribution requirements of an application is the third step of the material selection method.

4.2.1 Material Indices for Energy Absorption

A material index is developed for optimizing the material selection for an energy absorbing design by applying compliant mechanism theory to a single fold of the tessellation. The fold will be considered to be a small-length flexural pivot since it is much shorter and much more flexible than the panel. That is

$$L >> l \tag{4.1}$$

$$(EI)_L >> (EI)_l \tag{4.2}$$

where L is the length of the panel and l is the length of the fold in the direction of bending. By applying the Pseudo-Rigid-Body-Model (PRBM) approach [67], the small-length flexural pivot can be modeled as two rigid links that are pinned with a linear torsional spring between them.

The use of the small-length flexural pivot PRBM to model the fold also assumes a linear elastic material [85]. Creasing paper results in nonlinear stiffness at the folds [69, 86, 87]. The behavior of creases in other materials has also been evaluated [88]. Since the purpose of the material index is to assist in identifying non-paper materials that achieve elastic energy absorption, the strains are constrained to remain in the elastic range. Many materials can be modeled with reasonable accuracy to be linear in their elastic range. Therefore, the use of the small-length flexural pivot (PRBM) is acceptable, especially for purposes of early design decisions.

The objective of the material index is to identify materials which create a light, energy absorbent, small-length flexural pivot that is also constrained to stay elastic, $\sigma_{max} \leq \sigma_y$. The mass of the design is defined as:

$$m = btL\rho \tag{4.3}$$

where m is the mass, b is the base width, t is the thickness, L is the length of the panel, and ρ is the density of the material. The properties b, t, and L are a composite of four panels. Based on the Pseudo-Rigid-Body-Model approach, the energy stored in a torsional spring, U, is given by:

$$U = \frac{1}{2}K\theta^2 \tag{4.4}$$

K is the equivalent spring constant, defined as:

$$K = \frac{EI}{L} \tag{4.5}$$

where E is the modulus, and I is the section moment of inertia. θ is the angle of deflection given by:

$$\theta = \frac{ML}{EI} \tag{4.6}$$

where M is the moment applied. The yield strength, σ_y, is the maximum stress before yield occurs. At the point of yielding

$$\sigma_y = \frac{Mt}{2I} \tag{4.7}$$

Solving for M and substituting into equation (4.6) we obtain

$$\theta = \frac{2\sigma_y IL}{tEI} = \frac{2\sigma_y L}{tE} \tag{4.8}$$

and substituting equations (4.8) and (4.5) into equation (4.4) we obtain

$$U = \frac{1}{2}\left[\frac{EI}{L}\right]\left[\frac{2\sigma_y L}{tE}\right]^2 \tag{4.9}$$

Assuming a rectangular cross-section of the fold, $I = bt^3/12$, and distributing the square leads to an equation for energy absorbed before yielding:

$$U = \frac{Ebt^3 2^2 \sigma_y^2 L^2}{2[12][Lt^2 E^2]} = \frac{bt\sigma_y^2 L}{6E} \tag{4.10}$$

Simplifying and solving for t results in

$$t = \frac{6UE}{b\sigma_y^2 L} \tag{4.11}$$

Substituting equation (4.11) into equation (4.3) gives:

$$m = b \frac{6UE}{b\sigma_y^2 L}[L\rho] = \frac{6UE\rho}{\sigma_y^2} \qquad (4.12)$$

Eliminating constants yields the relationship of

$$m \ \alpha \ \frac{E\rho}{\sigma_y^2} \qquad (4.13)$$

Therefore, the material index for a light, energy absorbent unit cell is:

$$M_{index1} = \frac{\sigma_y^2}{E\rho} \qquad (4.14)$$

This material index shows that the ability of the Miura-ori to be light and to elastically absorb energy is dependent on the yield strength, Young's modulus and the density of the material.

Similarly, a material index for an inexpensive, energy absorbing design can be derived, where C_m is the material price per kg. The result is

$$M_{index2} = \frac{\sigma_y^2}{EC_m\rho} \qquad (4.15)$$

which shows the inverse relationship between the price of the material and its feasibility for this application. There is a trade-off between light and inexpensive that the designer must consider when choosing a suitable material.

These material indices can be used to identify suitable materials for the folds of the tessellation using Ashby material plots. They assume a linear elastic material for energy absorption. For materials with elastic properties with significant nonlinearities in the elastic range (e.g. hyperelastic materials), additional analysis would be required.

4.2.2 Finite Element Model

The material indices enable the selection of a class of materials that maximize the stored elastic energy in components with a general geometry. FEA is used to account for specific geometries, such as the Miura-ori and triangular corrugations (Figures 4.2 and 4.3), and to study material stiffness effects. If a mechanism based on the Miura-ori tessellation could be constructed to have perfectly flexible hinges and rigid panels, an applied load to the vertex of one unit cell
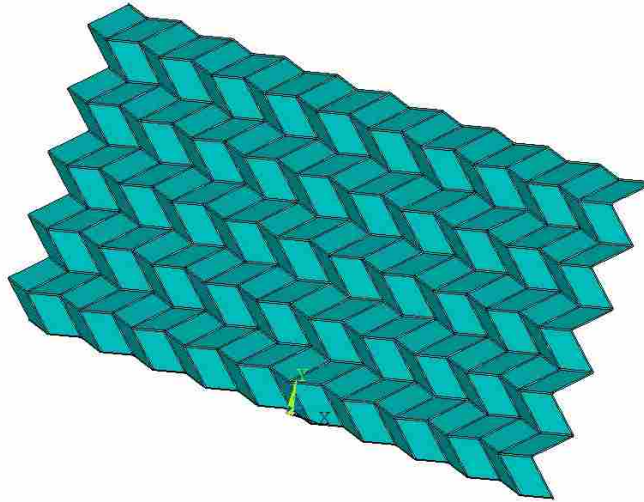
Figure 4.2: FEA model of a five-by-ten Miura-ori tessellation
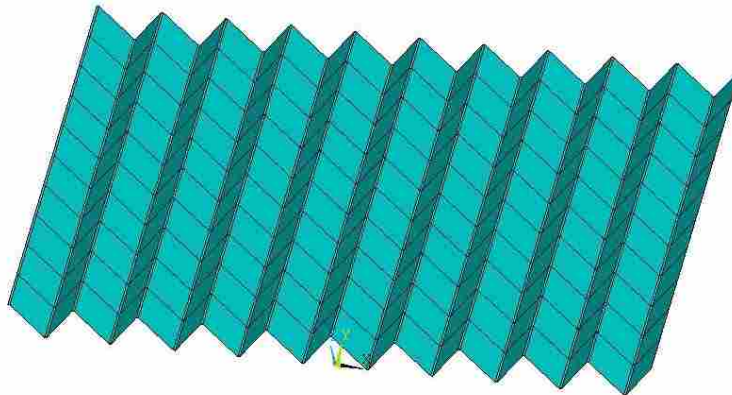
Figure 4.3: FEA model of a triangular wave corrugation.

would create a uniform deflection on each of the corresponding vertices of every unit cell across the tessellation. In the case of the triangular corrugation, rigid panels and flexible hinges would result in the deflection of just one of the corrugation peaks while the rest of the corrugation would remain undeflected.

In reality, the hinges are not perfectly flexible and the panels are not rigid, thus the deflection and the force that are transferred across the corrugations may decrease as a function of the distance from the loaded point. The *stiffness ratio*, *SR*, is defined to account for this nonideal
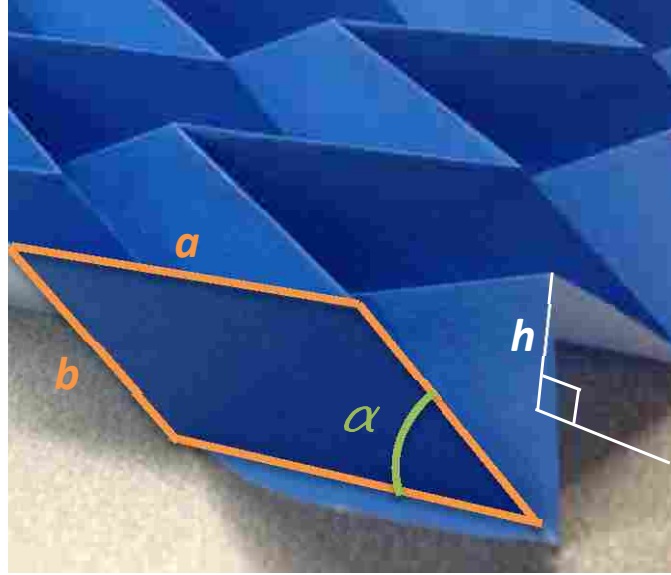
Figure 4.4: Dimensionsal paramaters Miura-ori unit cell.

behavior and is defined as the relative stiffness of the hinges to the stiffness of the panels. FEA was used to study the affects of this parameter on the deflection and force transfer characteristics of the Miura-ori and triangular corrugations.

The FEA was completed using a static, non-linear analysis in ANSYS. A five by ten tessellation (Figure 4.2) was constructed by using Shell181 elements. The dimensional parameters of the unit cell are shown in Figure 4.4. The lengths of *a* and *b* were both equal to 2.54 cm, the angle α was 45 degrees, the width of the hinges was 1/25 of the rhombus side length, and *h* was selected so that the panels would be 55 degrees from horizontal. The panels were meshed with a 25 x 25 element grid. The hinges were meshed with three elements across the hinge in order to more accurately model the highly localized deformations that occur there.

It was assumed that the main mode of deflection of the panels and hinges is in bending and therefore have a stiffness of *EI*. The relative stiffness of the panels and hinges can be controlled by assigning either different elastic moduli or area moments of inertia to the elements of the panels and hinges. For the purpose of this analysis, the moduli of the hinges were changed as a fraction of the moduli of the panels. Therefore, for this particular case the *stiffness ratio* is defined as:

$$SR = \frac{E_{hinge}}{E_{panel}} \qquad (4.16)$$

where E_{hinge} and E_{panel} are the modulli of the hinge and panel materials respectively. Analyses were run for stiffness ratios of 0.5, 0.1, 0.05, and 0.01. A displacement load in the vertical, Z-direction was applied to the central vertex. The loaded vertex was constrained from motion in the X and Y directions. All vertices interfacing with the $Z = 0$ plane were constrained to move in the X-Y plane. To simplify the model, a symmetry boundary condition was imposed to the nodes lying on the X-Z plane at Y=0.

A similar FEA was conducted using a model for a triangular corrugation as shown in Figure 4.3. The overall dimensions and corrugation height match those of the Miura-ori model as well as the loading and boundary conditions. These analyses allow for a comparison between the energy absorption and force distribution properties of a Miura-ori tessellation with those of a triangular corrugation.

The FEA is used to measure the applied force at the central vertex, the displacement of the top, unconstrained vertices and the reaction forces on the bottom ($Z = 0$), vertically-constrained vertices for the Miura-ori and the triangular corrugations. From the force and displacement data, we can calculate the energy absorbed by the corrugations and see the distribution of the transferred force. Typically, energy absorbing components should absorb the kinetic energy of a given force with a minimum peak force transferred through the component. A design that distributes the load well will have a smaller peak reaction force on the bottom of the pad compared to the applied load. Also, in addition to calculating the total energy absorbed for each *SR*, it will be desirable to also calculate the energy absorbed for a given force for each *SR*. This allows for the comparison of the Miura-ori and triangular corrugations for how efficiently they absorb energy based on *SR*.

4.3   Results and Discussion

4.3.1   Ashby Plots for Material Selection

The first step in the material selection process is to screen potential material choices based on their elastic strain value (S_y/E). Materials with an S_y/E value of less than 0.01 are not considered as they may not allow for enough elastic deflection and energy absorption required for many applications. The resultant set of materials are then plotted on Ashby charts with axes given by the critical material properties identified in the material indices developed above.
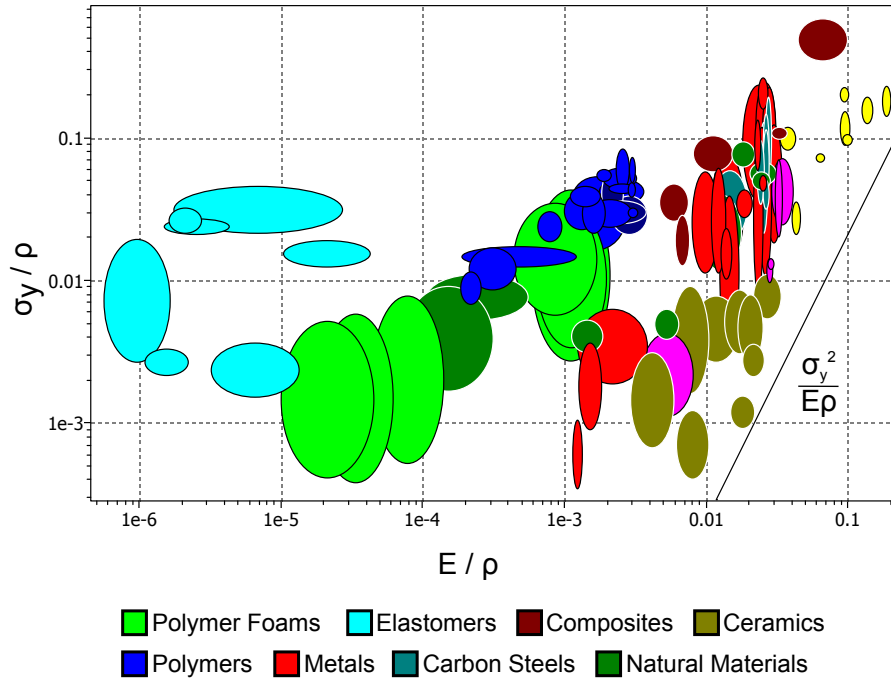
Figure 4.5: Ashby plot of specific yield strength vs. specific modulus.

The derived material indices provide a coupling of the individual material properties in a manner specific to achieving light weight, energy absorbing designs and cost effective, energy absorbing designs. Plotting the material properties with axes on a logarithmic scale allows specific values of the material indices to be plotted as linear contours. For example, the straight line in the bottom rigt corner of Figure 4.5 shows the slope of the line for constant values of the material index, M_{index1}, Eq. (4.14).

To achieve designs that are energy absorbent and light weight, the material index should be maximized. The value of the material index increases moving towards the top left of the chart, which would indicate that materials that lie in the top left corner would be good candidates. Some of the candidate materials would include Polyurethane, Isoprene, and Neoprene.

Figure 4.6 can be used with the second index, M_{index2}, Eq. (4.15), to identify materials for a cost effective, energy-absorbing design. Applying the same method to create contours for the material index, good candidates again lie in the top left corner of the chart. Some candidate materials for the case where an inexpensive, energy- absorbing material is the objective for an application are Polyurethane, Isoprene, Rubber, Polychloroprene, and EVA.

51
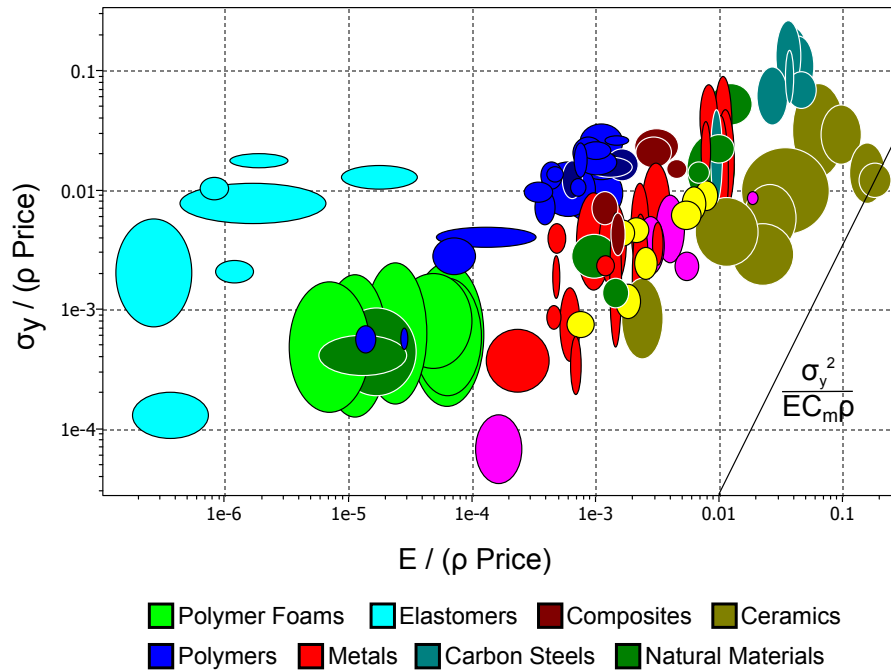
Figure 4.6: Ashby plot of specific yield strength vs. specific modulus with cost.

Designers would also need to take other factors into consideration while making a material selection. For example, while a raw material may be inexpensive, the manufacturing process needed to produce the final design will also affect the cost. Also, since energy absorption requires that the design handle multiple impacts, the fracture toughness and fatigue life of a material may be considered.

4.3.2 Detailed Local Material Selection and Design

A critical factor that determines how well a mechanism based on origami tessellations will absorb energy and distribute applied forces is the relative stiffness between the tessellated faces and the folded or hinged joints. The stiffness of a panel or a beam under bending can be changed by either changing its material properties (elastic modulus) or its geometry (area moment of inertia).

FEA was used to study the force and deflection characteristics of the Miura-ori as a function of the stiffness ratio, *SR*, Eq. (4.16). The three-dimensional displacement of the top, unconstrained vertices for a stiffness ratio of 0.01 and of 0.5 are shown in Figure 4.7. A decrease in the stiffness ratio results in greater auxetic expansion, which coincides with greater vertical displacement of

(a) $SR = 0.01$ (b) $SR = 0.5$
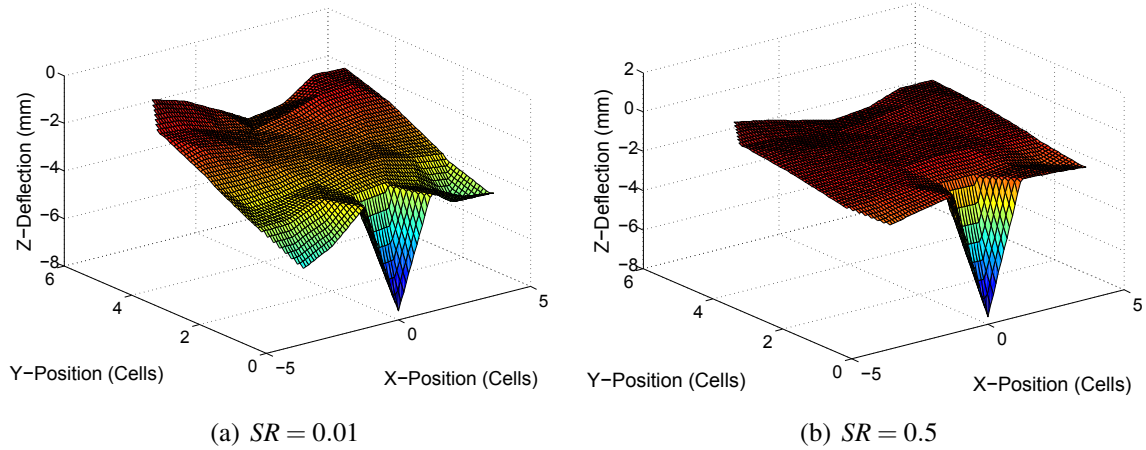
Figure 4.7: Three-dimensional displacement of the top vertices.

the top vertices across the tessellation. If the panels were perfectly rigid and the hinges flexible, resulting in $SR = 0$, a surface plot of the vertex displacements would be perfectly flat, with every vertex moving the same amount in the vertical direction across the tessellation. Figure 4.8 shows the effect of SR on the average vertical displacement as a function of the distance from the load. A lower stiffness ratio results in greater vertical displacement throughout the tessellation.

The reaction force on the central, loaded, vertex is plotted as a function of its percent deflection for each of the four stiffness ratios in Figure 4.9. The percent deflection ($\%h$) is defined as

$$\%h = \frac{h}{h_0} * 100 \tag{4.17}$$

where h is the vertical height of the central vertex and h_0 is the starting height of the central vertex. An interesting result is the linear nature of these force-deflection curves. This would indicate that unlike many foams, the entire Miura-ori tessellation behaves as an equivalent linear spring. This allows for simple analysis of the elastic energy absorption for mechanisms based on the Muira-ori. The results show that a higher SR results in greater reaction forces on the central vertex. However, a lower SR results in greater auxetic expansion of the tessellation.

Integrating the force-deflection data results in a plot of the energy absorbed as a function of displacement, as presented in Figure 4.10. This shows that for a given displacement, increasing the SR results in higher energy absorption; this simply reflects the fact that a stiffer component

53
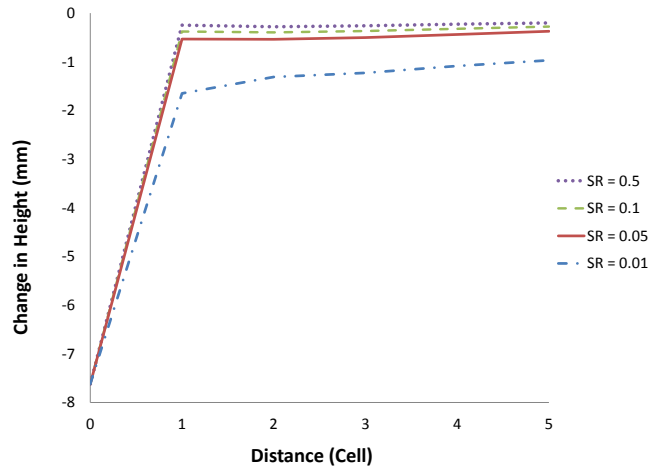
Figure 4.8: Vertical displacement of top vertices as a function of distance from central vertex for each *SR*.
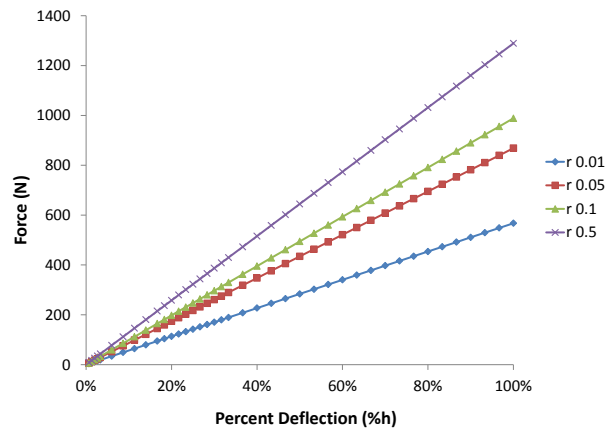
Figure 4.9: Reaction force on central vertex vs. vertical displacement for each *SR*.

will absorb more energy for a given displacement. As mentioned, however, a more meaningful comparison for energy absorption applications would be to compare the energy absorbed for a given force rather than a given displacement. If a particular force is selected, and the energy absorption calculated for each *SR* at that force, we can compare the energy absorption as a function of *SR*, as presented in Figure 4.11.

It can be seen that lower *SR* corresponds to greater energy absorbed for a given force in both the Miura-ori and triangular corrugations. However, the change in the energy absorbed is much
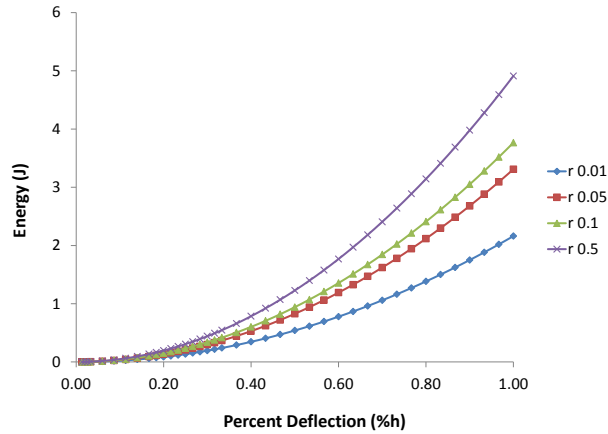
Figure 4.10: Absorbed energy as a function of vertical displacement of central vertex for each *SR*.
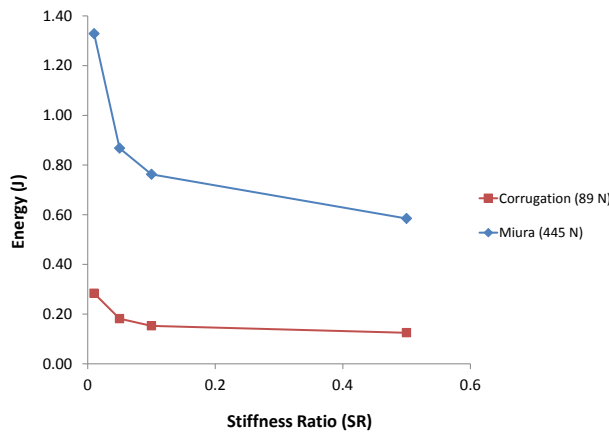
Figure 4.11: Absorbed energy for a given force as a function of stiffness ratio.

greater in the Miura-ori than the triangular corrugation. Since a lower stiffness ratio corresponds to more energy absorption for a given force and greater auxetic expansion of the tessellation, it is reasonable to conclude that the auxetic expansion of the tessellation is a mechanism for more efficient energy absorption, especially when compared to a basic triangular corrugation that expands much less.

Another important function of energy absorbing devices is their ability to distribute an applied load over a larger area. The reaction forces on the bottom vertices of the tessellation

were compared for each *SR*. The ability of the corrugation to distribute a force can be defined by evaluating a parameter referred to in this paper as the *force ratio*, FR, such that

$$FR = \frac{F_{max}}{F_{applied}} \tag{4.18}$$

where F_{max} is the maximum of the reaction forces acting on the vertices in the Z=0 plane and $F_{applied}$ is the force applied to the central vertex estimated as the sum of the reaction forces. A larger value of FR indicates a bigger difference between the maximum force at any point under the tessellation and the applied force. This will be the case if the force is not well-distributed across the sheet. Figure 4.12 shows this force ratio as a function of the stiffness ratio for the Miura-ori and the triangular corrugation. It can be seen that a larger stiffness ratio results in increased force distribution. Also, the FR of the Miura-ori is much greater than that of the triangular corrugation indicating greater force distribution.

Changing the stiffness ratio results in opposing effects on energy absorption and force distribution. A reduction in the *SR* to increase energy absorption produces a tessellation that is less effective at distributing an applied load. It is therefore necessary for designers to evaluate the specific application and select the *SR* that will result in the desired balance between energy absorption and force distribution.

It should be noted that the FR is a non-dimensional parameter used for comparing the effects of changing the *SR*. It is dependent on the boundary conditions of the FEA. The bottom vertices of the tessellated sheet were constrained in the vertical direction which resulted in some negative reaction forces. These negative forces generally occurred at the same vertices for each *SR* analysis and were accounted for in the estimation of $F_{applied}$ for each *SR*.

4.3.3   Application Example

The following section provides an example of how this method could be applied to select a material for use in an origami-inspired, compliant corrugation for energy absorption. One potential application of a Miura-ori sheet would be as padding inside a shipping box to protect an item such as a laptop computer. The desired function of the design is to be lightweight and energy absorbent.
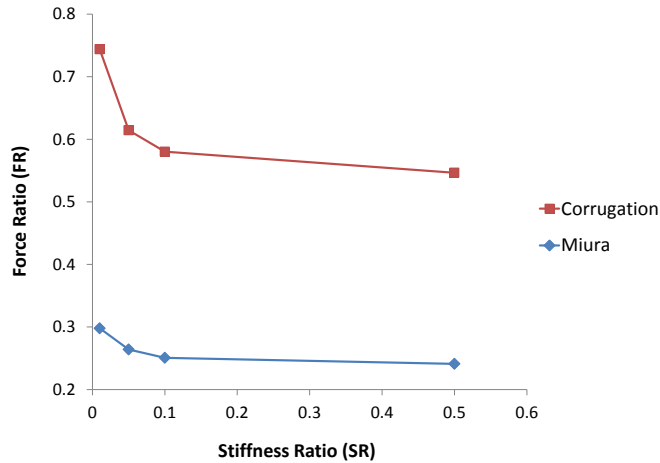
Figure 4.12: Reaction force ratio as a function of stiffness ratio.

First, materials are filtered according to their elastic strain and modulus. To allow for deflection of the compliant joints or hinges in the tessellated sheet, it is preferable that the material have an elastic strain greater than 0.01. Also, the tessellation panels should resist deflection, so materials are additionally filtered to eliminate any with an elastic modulus below 100 MPa. In this example, this is done using the material database, CES Edupack.

The subset of materials is then plotted on an Ashby plot as shown in Figure 4.13. A contour line of constant values of the material index M_{index1} is plotted to aid in identifying the materials that maximize the index where the contours increase from right to left. Figure 4.13 shows four possible materials in the maximum region. Leather could be eliminated as not being cost effective, which leaves three polymers; Ionomers, PTFE and Thermoplastics. The final selection could be made based on other design factors such as manufacturability, availability, cost, etc.

The last material-related design decision to make is selecting a stiffness ration, SR, for the tessellation. To protect a laptop computer during shipping, energy absorption as well as distribution of impact forces are needed. A smaller SR will absorb more energy while a larger SR will distribute forces. By evaluating the energy and force ratio plots from the FEA (Figures 4.11 and 4.12), it can be seen that a SR of 0.05 provides a large amount of energy absorption without significantly changing its FR and is therefore a good compromise between the competing objectives. A possible implementation of the stiffness ratio in the design would be to make the thickness of the material
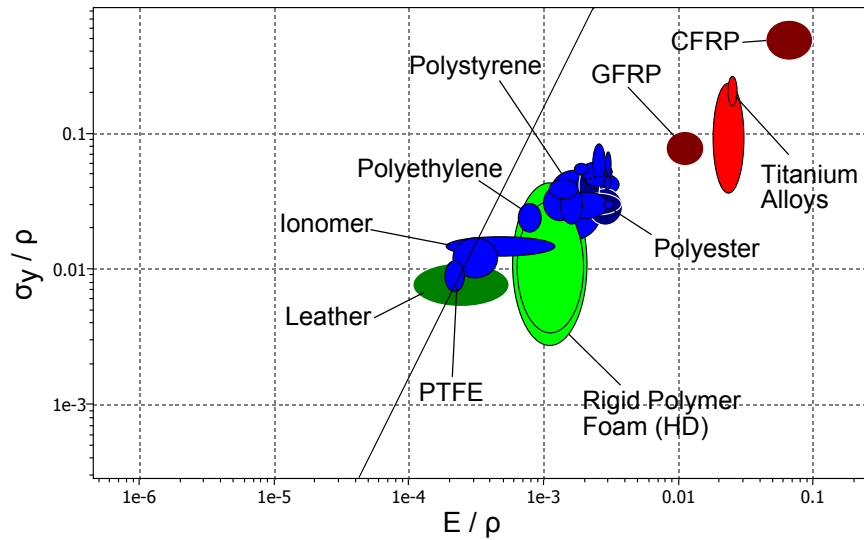
Figure 4.13: Material selection plot after screening based on elastic strain and modulus.

in the joint or hinge about 37% of the thickness of the panel. Additionally, some space would need to be allowed around the edges of the Miura-ori padding to allow for some in-plane expansion of the sheet under load.

4.4 Conclusions

There are many applications where elastic energy absorption and force distribution are needed. The unique mechanical properties of some origami-inspired mechanisms based on folded tessellations, such as the Miura-ori pattern, may prove useful in these applications. Since these mechanisms rely on the deformation of their folds or hinges to achieve their motion, they are considered compliant mechanisms and can be analysed by applying compliant mechanism theory. This study has investigated some material-related issues pertaining to the design of origami-inspired elastic energy absorption and force distribution mechanisms which had previously not been studied. A three-step method was presented for selecting materials for origami-inspired compliant corrugations.

The material indices derived can enable the identification of materials that will either be light and energy absorbent, or cost effective and energy absorbent. These material indices can

be used with Ashby plots of many materials to identify the materials which optimize the material indices.

The stiffness ratio is defined as the relative stiffness of the folds or compliant hinges to the panels and is helpful in addressing the nonideal behavior of the system. Using finite element analysis, this stiffness ratio was found to affect both the energy absorption and force distribution characteristics of the Miura-ori tessellation. A lower stiffness ratio allows for more auxetic expansion of the mechanism which results in greater energy absorption. A higher stiffness ratio will distribute an applied force across more of the tessellated sheet.

The stiffness ratio can be varied by changing the modulus of the hinge elements relative to the panel elements or by adjusting the material thickness, thereby changing the moment of inertia of the two areas. For designers, both options may be available for creating the desired stiffness ratio. A tessellation could be created by using two different materials for the hinges and panels. This would allow the sheet to have a consistent cross sectional thickness. Alternatively, a single material could be used and manufactured or processed to create a different thickness at the hinges compared to the panels. This may be achieved through machining, molding, for other forming operations.

While the methods and analyses developed in this study focus specifically on the Miura-ori pattern, they may be applied to other origami tessellations when used in mechanisms for energy absorption or force distribution.

Other factors relating to the elastic energy absorbing characteristics of origami tessellations should be considered in future work. It will be important to study the geometric effects of the tessellated shape; both changes to a given base shape and comparing different tessellated patterns. Also, the dynamic effects of impacts on energy absorption and force distribution for origami tessellations should be studied. The auxetic motion of origami tessellations may have other benefits when used for energy absorption. For example, attaching an energy absorbing membrane to the tessellation and straining it through the auxetic expansion, is a concept that will also be pursued in future work.

CHAPTER 5.   CONCLUSION

Compliant corrugations may provide useful means for engineers to absorb kinetic energy in certain applications. An innovative padding concept was investigated that may be useful to meet the needs of athletes to provide a light, effective padding that protects them from impact injuries and does not interfere with their ability to compete in their sport. It was found that the type of wave shape of the corrugation may not be a major factor in the energy absorption and that the best performance of a corrugation for elastic energy absorption is achieved when the wave has peak-to-peak height and length that are equal.

The adaptation of origami tessellations to create new corrugation configurations shows promise for energy absorption applications. Analytical models were developed to investigate how the geometrical parameters of the Miura-ori tessellation affect its elastic energy absorption properties. It was found that the starting height of the central vertex of the unit cell affects the shape of its force-deflection response. The effects of the side lengths and the interior acute angle of the tessellated parallelogram of the Miura-ori were also investigated. It was found that energy absorption and peak force tended to increase with increasing a/b and decreasing α with the exception that for the membrane model, more energy is absorbed in the midrange α between 40 and 60 degrees.

A three-step method was presented for selecting materials for origami-inspired compliant corrugations. First, materials are screened based on their elastic strain and modulus values. Second, the Ashby method is applied as a means to refine the choice of material further by optimizing particular properties of the final component (such as mass, cost, resilience). Third, specific stiffness characteristics are chosen to deliver improved force distribution and energy absorption properties for a peak desired force transfer.

Auxetic expansion is a efficient means of absorbing energy. Using finite element analysis, the stiffness ratio was found to affect both the energy absorption and force distribution characteristics of the Miura-ori tessellation. A lower stiffness ratio allows for more auxetic expansion of

the mechanism which results in greater energy absorption. A higher stiffness ratio will distribute an applied force across more of the tessellated sheet. Furthermore, the Miura-ori tessellation was shown to have both better energy absorption and force distribution abilities when compared to a triangular wave corrugation. The ANSYS batch files used for the FEA are included in Appendix A.

While the models, methods and analyses developed in this research focus specifically on the Miura-ori pattern, they may be applied to other origami tessellations when used in compliant corrugations for energy absorption.

5.1 Summary of Contributions

The primary contributions of this research are:

1. Modeling and testing of a corrugated padding concept.

2. Improved understanding of wave shape effects on energy absorption of compliant corrugations.

3. Derivation and verification of kinetic models of two energy-absorbing modes of the Miura-ori unit cell.

4. Analyses showing advantages of auxetic expansion.

5. Development of a material selection process for origami-inspired compliant corrugations.

5.2 Suggested Future Work

Further development of the corrugated padding concept will increase its attractiveness as a commercially viable product. A key advantage of the concept is provided by the mechanical behavior of the corrugation. Corrugating a sheet of material increases its bending stiffness in one direction while maintaining a lower bending stiffness in another direction. This idea may be exploited to produce padding specific to a certain body part and motion. Other corrugation shapes may also prove beneficial for certain motions or applications. For example, rather than a straight corrugation, curved or orthogonal corrugations may also be beneficial. Also, other materials and

manufacturing processes may be investigated that would produce lighter designs while still providing a desired level of protection.

Another feature of the corrugated padding concept is the soft outer surface resulting from the harder wave being embedded in a softer foam. A soft surface pad when worn for protection during a impact sport, may provide additional protection to opposing athletes. For example, it has been shown that a softer shoulder pad in hockey may lower the risk of concussions for players in helmet to shoulder contacts [89]. Further research is warranted to explore such advantages.

This work lays a theoretical foundation for the use of the Miura-ori or similar origami tessellations in energy absorption applications. Further work could be done to investigate how the models could be used to "tune" an energy absorption device based on the Miura-ori to achieve application-specific force deflection curves.

During the course of this research, several prototypes were built and many manufacturing difficulties and hardware limitations were encountered. As a summer project, an attempt was made to build an energy absorbing pad (called a *crash pad*) that could be used for the *bouldering* style of rock climbing. The final report of that project is included in Appendix B in order to capture the lessons learned. More exploration of materials and manufacturing processes to build mechanisms that achieve the desired motion while also absorbing energy will be necessary.

The analyses of the origami-based mechanisms in this research centered on a quasi-static approach. However, most applications for such designs will be highly dynamic, impact situations. Therefore, he dynamic effects of impacts on energy absorption and force distribution for origami tessellations should be studied.

Lastly, the affects of combining unit cells in different configurations should be studied. Some configurations could include stacking tessellated sheets in a mirrored (peak-to-peak) or aligned (peak-to-valley) configuration. Some testing done as part of this research suggests a peak-to-peak stacking may provide additional mechanical advantage to increase the auxetic expansion of the tessellated sheet. Future work in this area may provide new insights into potential uses of these designs.

REFERENCES

[1] Howell, L. L., 2001. *Compliant mechanisms*. Wiley-Interscience. 2, 22, 25

[2] Ashby, M. F., 2011. *Materials Selection in Mechanical Design*. Butterworth-Heinemann. 3, 43

[3] Nichols, E. H., and Richardson, F. L., 2003. "The classic: Football injuries of the harvard squad for three years under the revised rules.::" *Clinical Orthopaedics and Related Research,* **409**, Apr., pp. 3–10. 4

[4] McIntosh, A. S., 2012. "Biomechanical considerations in the design of equipment to prevent sports injury." *Proceedings of the Institution of Mechanical Engineers, Part P: Journal of Sports Engineering and Technology,* **226**(3-4), Sept., pp. 193–199. 4

[5] Gerrard, D. D. F., 1998. "The use of padding in rugby union." *Sports Medicine,* **25**(5), May, pp. 329–332. 4

[6] Marshall, S. W., Loomis, D. P., Waller, A. E., Chalmers, D. J., Bird, Y. N., Quarrie, K. L., and Feehan, M., 2005. "Evaluation of protective equipment for prevention of injuries in rugby union." *International Journal of Epidemiology,* **34**(1), Feb., pp. 113–118 PMID: 15561749. 4

[7] McIntosh, A. S., Patton, D. A., and Thai, K., 2012. "Impact assessment of jockey helmet liner materials." *Proceedings of the Institution of Mechanical Engineers, Part P: Journal of Sports Engineering and Technology,* **226**(3-4), Sept., pp. 237–243. 4, 5

[8] Marshall, S. W., Waller, A. E., Dick, R. W., Pugh, C. B., Loomis, D. P., and Chalmers, D. J., 2002. "An ecologic study of protective equipment and injury in two contact sports." *International Journal of Epidemiology,* **31**(3), June, pp. 587–592 PMID: 12055160. 4

[9] Mitchell, B., 2000. "Efficacy of thigh protectors in preventing thigh haematomas." *Journal of Science and Medicine in Sport,* **3**(1), Mar., pp. 30–34. 4

[10] Rousseau, P., Post, A., and Hoshizaki, T. B., 2009. "The effects of impact management materials in ice hockey helmets on head injury criteria." *Proceedings of the Institution of Mechanical Engineers, Part P: Journal of Sports Engineering and Technology,* **223**(4), Dec., pp. 159–165. 4, 5

[11] Yang, J., Marshall, S. W., Bowling, J. M., Runyan, C. W., Mueller, F. O., and Lewis, M. A., 2005. "Use of discretionary protective equipment and rate of lower extremity injury in high school athletes." *American Journal of Epidemiology,* **161**(6), Mar., pp. 511–519 PMID: 15746467. 4

[12] Williams-Avery, R. M., and Mackinnon, D. P., 1996. "Injuries and use of protective equipment among college in-line skaters." *Accident Analysis & Prevention,* **28**(6), Nov., pp. 779–784. 4

[13] NFL: players must wear thigh, knee pads in '13. 4

[14] Liew, K., Peng, L., and Kitipornchai, S., 2007. "Nonlinear analysis of corrugated plates using a FSDT and a meshfree method." *Computer Methods in Applied Mechanics and Engineering,* **196**(2124), Apr., pp. 2358–2376. 4, 5

[15] Shimansky, R. A., and Lele, M. M., 1995. "Transverse stiffness of a sinusoidally corrugated plate*." *Mechanics of Structures and Machines,* **23**(3), pp. 439–451. 4

[16] He, L., Cheng, Y.-S., and Liu, J., 2012. "Precise bending stress analysis of corrugated-core, honeycomb-core and x-core sandwich panels." *Composite Structures,* **94**(5), Apr., pp. 1656–1668. 5

[17] Gilchrist, A. C., Suhling, J. C., and Urbanik, T. J., 1998. "Nonlinear finite element modeling of corrugated board." *ASME APPLIED MECHANICS DIVISION-PUBLICATIONS-AMD,* **231**, p. 101106. 5

[18] Briassoulis, D., 1986. "Equivalent orthotropic properties of corrugated sheets." *Computers & Structures,* **23**(2), pp. 129–138. 5

[19] Biancolini, M., 2005. "Evaluation of equivalent stiffness properties of corrugated board." *Composite Structures,* **69**(3), July, pp. 322–328. 5

[20] Buannic, N., Cartraud, P., and Quesnel, T., 2003. "Homogenization of corrugated core sandwich panels." *Composite Structures,* **59**(3), Feb., pp. 299–312. 5

[21] Kress, G., and Winkler, M., 2010. "Corrugated laminate homogenization model." *Composite Structures,* **92**(3), Feb., pp. 795–810. 5

[22] Kress, G., and Winkler, M., 2011. "Corrugated laminate analysis: A generalized plane-strain problem." *Composite Structures,* **93**(5), Apr., pp. 1493–1504. 5

[23] Luo, S., Suhling, J. C., Considine, J. M., and Laufenberg, T. L., 1992. "The bending stiffnesses of corrugated board." *Mechanics of Cellulosic Materials.* 5

[24] Reany, J., and Grenestedt, J. L., 2009. "Corrugated skin in a foam core sandwich panel." *Composite Structures,* **89**(3), July, pp. 345–355. 5

[25] Talbi, N., Batti, A., Ayad, R., and Guo, Y., 2009. "An analytical homogenization model for finite element modelling of corrugated cardboard." *Composite Structures,* **88**(2), Apr., pp. 280–289. 5

[26] Wennberg, D., Wennhage, P., and Stichel, S., 2011. "Orthotropic models of corrugated sheets in finite element analysis." *ISRN Mechanical Engineering,* **2011**. 5

[27] Winkler, M., and Kress, G., 2012. "Influence of corrugation geometry on the substitute stiffness matrix of corrugated laminates." *Composite Structures,* **94**(9), Sept., pp. 2827–2833. 5

[28] Xia, Y., Friswell, M. I., and Saavedra Flores, E. I., 2012. "Equivalent models of corrugated panels." *International Journal of Solids and Structures,* **49**(13), June, pp. 1453–1462 WOS:000304744400003. 5

[29] Zhang, J., Qin, Q., and Wang, T. J., 2012. "Compressive strengths and dynamic response of corrugated metal sandwich plates with unfilled and foam-filled sinusoidal plate cores." *Acta Mechanica*, p. 117. 5

[30] Rueda, M. A. F., and Gilchrist, M. D., 2012. "Computational analysis and design of components of protective helmets." *Proceedings of the Institution of Mechanical Engineers, Part P: Journal of Sports Engineering and Technology,* **226**(3-4), Sept., pp. 208–219. 5

[31] Blanco, D. H., Cernicchi, A., and Galvanetto, U., 2014. "Design of an innovative optimized motorcycle helmet." *Proceedings of the Institution of Mechanical Engineers, Part P: Journal of Sports Engineering and Technology*, Jan., p. 1754337113518748. 5

[32] Mills, N. J., 2006. "Finite element models for the viscoelasticity of open-cell polyurethane foam." *Cellular polymers,* **25**(5), p. 293316. 5

[33] Burbank, S. D., and Smith, L. V., 2012. "Dynamic characterization of rigid foam used in finite element sports ball simulations." *Proceedings of the Institution of Mechanical Engineers, Part P: Journal of Sports Engineering and Technology,* **226**(2), Apr., pp. 77–85. 5

[34] LS-Dyna, 2012. Livermore software technology corporation. 7

[35] Autodesk Inventor Professional 2014, 2013. Autodesk, Inc. 7

[36] LS-PrePost, 2012. Livermore Software Technology Corporation. 7

[37] Francisco, A. C., Nightingale, R. W., Guilak, F., Glisson, R. R., and Garrett, W. E., 2000. "Comparison of soccer shin guards in preventing tibia fracture." *The American journal of sports medicine,* **28**(2), p. 227233. 9

[38] Desmoulin, G. T., and Anderson, G. S., 2011. "Method to investigate contusion mechanics in living humans." *Journal of Forensic Biomechanics,* **2**(online), p. 110. 13

[39] Bathe, K.-J., and Bathe, K.-J., 2006. *Finite element procedures*. s.n.], S.l. 16

[40] Bowen, L. A., Grames, C. L., Magleby, S. P., Howell, L. L., and Lang, R. J., 2013. "A classification of action origami as systems of spherical mechanisms." *Journal of Mechanical Design,* **135**(11), p. 111008. 19, 22

[41] Miura, K., 1972. "Zeta-core sandwich- its concept and realization." *Inst. of Space and Aeronautical Science, Univer sity of Tokyo*(480), p. 137164. 19, 20, 42

[42] Klett, Y., and Drechsler, K., 2011. "Designing technical tessellations." *International Meeting of Origami Science, Mathematics, and Education,* **5**, pp. 305–322. 20, 41

[43] Lebe, A., and Sab, K., 2012. "Homogenization of thick periodic plates: Application of the bending-gradient plate theory to a folded core sandwich panel." *International Journal of Solids and Structures,* **49**(1920), Oct., pp. 2778–2792. 20

[44] Miura, K., 1980. "Method of packaging and deployment of large membranes in space." In *31st Congress of the International Astronautical Federation*. 20

[45] Kobayashi, H., Kresling, B., and Vincent, J. F., 1998. "The geometry of unfolding tree leaves." *Proceedings of the Royal Society of London. Series B: Biological Sciences,* **265**(1391), p. 147154. 20

[46] Tachi, T., 2009. "Generalization of rigid foldable quadrilateral mesh origami." In *Symposium of the International Association for Shell and Spatial Structures (50th. 2009. Valencia). Evolution and Trends in Design, Analysis and Construction of Shell and Spatial Structures: Proceedings*. 21, 41, 42

[47] Stachel, H., 2009. "Remarks on miura-ori, a japanese folding method." In *International Conference on Engineering Graphics and Design*, Vol. 12, p. 13. 21, 42

[48] Stachel, H., 2010. "A kinematic approach to kokotsakis meshes." *Computer Aided Geometric Design,* **27**(6), p. 428437. 21

[49] Stachel, H., 2011. "Remarks on flexible quad meshes." *Proc. BALTGRAF-11, Eleventh Internat. Conference, Tallinn/Estonia*. 21, 42

[50] Schenk, M., and Guest, S. D., 2010. "Folded textured sheets." In *Symposium of the International Association for Shell and Spatial Structures (50th. 2009. Valencia). Evolution and Trends in Design, Analysis and Construction of Shell and Spatial Structures: Proceedings*. 21

[51] Schenk, M., and Guest, S. D., 2011. "Origami folding: A structural engineering approach." In *Origami 5: Fifth International Meeting of Origami Science, Mathematics, and Education (5OSME)*, p. 291303. 21, 42

[52] Schenk, M., and Guest, S. D., 2013. "Geometry of miura-folded metamaterials." *Proceedings of the National Academy of Sciences of the United States of America,* **110**(9), Feb., pp. 3276–3281 WOS:000315841900024. 21, 31

[53] Gattas, J. M., Wu, W., and You, Z., 2013. "Miura-base rigid origami: Parameterizations of first-level derivative and piecewise geometries." *Journal of Mechanical Design,* **135**(11), Oct., p. 111011. 21

[54] Tolman, S. S., Beatty, A. M., Bowden, A. E., and Howell, L. L., 2014. "Parameter characterization for elastic energy absorption of an embedded corrugated wave padding concept with sports applications." *Journal of Sports Engineering and Technology,* **In Press**. 21, 39

[55] Greenberg, H. C., Gong, M. L., Magleby, S. P., and Howell, L. L., 2011. "Identifying links between origami and compliant mechanisms." *Mechanical Sciences,* **2**. 22

[56] Chiang, C. H., 2000. *Kinematics of spherical mechanisms*. Krieger Pub., Malabar, FL. 22

[57] Cervantes-Snchez, J. J., and Medellin-Castillo, H. I., 2002. "A robust classification scheme for spherical 4< i> r</i> linkages." *Mechanism and machine theory,* **37**(10), p. 11451163. 22

[58] Lang, R. J., 2001. Tessellations and twists. 22, 23, 24

[59] Ma, J., and You, Z., 2013. "Energy absorption of thin-walled square tubes with a prefolded origami PatternPart i: Geometry and numerical simulation." *Journal of Applied Mechanics,* **81**(1), Aug., p. 011003. 22

[60] Ma, J., and You, Z., 2013. "A novel origami crash box with varying profiles." ASME, p. V06BT07A048. 22

[61] Ma, J., and You, Z., 2011. "The origami crash box." *Origami,* **5**, p. 277290. 22

[62] Gattas, J. M., and You, Z., 2013. "Quasi-static impact response of alternative origami-core sandwich panels." ASME, p. V06BT07A032. 22

[63] Basily, B. B., and Elsayed, E. A., 2004. "Dynamic axial crushing of multilayer core structures of folded chevron patterns." *International Journal of Materials & Product Technology,* **21**(1-3), pp. 169–185. 22, 42

[64] Audoly, B., and Boudaoud, A., 2008. "Buckling of a stiff film bound to a compliant substratePart III:: herringbone solutions at large buckling parameter." *Journal of the Mechanics and Physics of Solids,* **56**(7), p. 24442458. 22, 42

[65] Heimbs, S., Cichosz, J., Klaus, M., Kilchert, S., and Johnson, A., 2010. "Sandwich structures with textile-reinforced composite foldcores under impact loads." *Composite Structures,* **92**(6), May, pp. 1485–1497. 22, 42

[66] Heimbs, S., 2013. "Foldcore sandwich structures and their impact behaviour: An overview." In *Dynamic Failure of Composite and Sandwich Structures*. Springer, p. 491544. 22, 42

[67] Howell, L. L., 2001. *Compliant Mechanisms*. John Wiley & Sons, Inc. 27, 43, 45

[68] Mentrasti, L., Cannella, F., Pupilli, M., and Dai, J. S., 2013. "Large bending behavior of creased paperboard. II. structural analysis." *International Journal of Solids and Structures,* **50**(2021), Oct., pp. 3097–3105. 29

[69] Mentrasti, L., Cannella, F., Pupilli, M., and Dai, J. S., 2013. "Large bending behavior of creased paperboard. i. experimental investigations." *International Journal of Solids and Structures,* **50**(20), p. 30893096. 29, 45

[70] Giampieri, A., Perego, U., and Borsari, R., 2011. "A constitutive model for the mechanical response of the folding of creased paperboard." *International Journal of Solids and Structures,* **48**(1617), Aug., pp. 2275–2287. 29

[71] Ge, Q., Luo, X., Iversen, C. B., Nejad, H. B., Mather, P. T., Dunn, M. L., and Jerry Qi, H., 2014. "A finite deformation thermomechanical constitutive model for triple shape polymeric composites based on dual thermal transitions." *International Journal of Solids and Structures,* **51**(1516), Aug., pp. 2777–2790. 40

[72] Zirbel, S. A., Lang, R. J., Magleby, S. P., Thomson, M. W., Sigel, D. A., Walkemeyer, P. E., Trease, B. P., and Howell, L. L., 2013. "Accommodating thickness in origami-based deployable arrays." *Journal of Mechanical Design*. 41

[73] Kruibayashi, K., Tsuchita, K., You, Z., Tomus, D., Umemoto, M., Ito, T., and Sasaki, M., 2006. "Self-deployable origami stent grafts as a biomedical application of ni-rich tini shape memory alloy foil." *Materials Science and Engineering: A,* **419**, pp. 131–137. 41

[74] Daynes, S., Grisdale, A., Seddon, A., and Trask, R., 2014. "Morphing structures using soft polymers for active deployment." *Smart Materials and Structures,* **23**(1), Jan., p. 012001. 41

[75] Schenk, M., and Guest, S. D., 2011. "Origami folding: A structural approach." *International Meeting of Origami Science, Mathematics, and Education,* **5**, pp. 291–303. 41

[76] Wu, W., and You, Z., 2010. "Modeling rigid origami with quaternions and dual quaternions." *Proceedings of the Royal Society,* **466**, pp. 2155–2174. 41

[77] Virk, K., Monti, A., Trehard, T., Marsh, M., Hazra, K., Boba, K., Remillat, C. D. L., Scarpa, F., and Farrow, I. R., 2013. "SILICOMB PEEK kirigami cellular structures: mechanical response and energy dissipation through zero and negative stiffness." *Smart Materials and Structures,* **22**(8), Aug., p. 084014. 42

[78] Greenberg, H. C., Gong, M. L., Magleby, S. P., and Howell, L. L., 2011. "Identifying links between origami and compliant mechanisms." *Mechanical Sciences,* **2**, pp. 217–225. 43

[79] Lu, G., and Yu, T., 2003. *Energy Absorption of Structures and Materials*. Woodhead Publishing Ltd and CRC press LLC. 43

[80] Sun, D. X., and Zhao, Y. Y., 2003. "Static and dynamic energy absorption of al foams produced by the sintering and dissolution process." *Metallurgical and Materials Transactions B: Process Metallurgy and Materials Processing Science,* **v. 34**, pp. 69–74. 43

[81] Gouker, R. M., Gupta, S. K., Bruck, H. A., and Holzschuh, T., 2006. "Manufacturing of multi-material compliant mechanisms using multi-material molding." *The International Journal of Advanced Manufacturing Technology,* **30**(11-12), Oct, pp. 1049–1075. 43

[82] Vogtmann, D. E., Gupta, S. K., and Bergbreiter, S., 2011. "Multi-material compliant mechanisms for mobile millirobots." In *IEEE International Conference on Robotics and Automation*, IEEE. 43

[83] Hegde, S., and Ananthasuresh, G. K., 2010. "Design of single-input-single-output compliant mechanisms for practical applications using selection maps." *Journal of Mechanical Design,* **132**, August. 43

[84] Balkcom, D. J., and Mason, M. T., 2008. "Robotic origami folding." *The International Journal of Robotics Research,* **27**, pp. 613–627. 44

[85] Howell, L. L., and Midha, A., 1994. "A method for the design of compliant mechanisms with small-length flexural pivots." *Journal of Mechanical Design,* **116**(1), p. 280290. 45

[86] Dai, J. S., and Cannella, F., 2008. "Stiffness characteristics of carton folds for packaging." *Journal of mechanical design,* **130**(2), p. 022305. 45

[87] Nagasawa, S., BIN, M. M. N., and Shiga, Y., 2011. "Bending moment characteristics on repeated folding motion of coated paperboard scored by round-edge knife." *Journal of Advanced Mechanical Design, Systems, and Manufacturing,* **5**(4), p. 385394. 45

[88] Francis, K.C., Blanch, J.E, Magleby, S.P, and Howell, L.L, 2013. "Origami-like creases in sheet materials for compliant mechanism design." *Mechanical Sciences,* **4**, pp. 371–380. 45

[89] Kendall, M., Post, A., Rousseau, P., and Hoshizaki, T. B., 2014. "The effect of shoulder pad design on reducing peak resultant linear and rotational acceleration in shoulder-to-head impacts." In *Mechanism of Concussion in Sports*, A. Ashare and M. Ziejewski, eds. ASTM International, 100 Barr Harbor Drive, PO Box C700, West Conshohocken, PA 19428-2959, June, pp. 1–11. 62

APPENDIX A.   ANSYS BATCH FILES

This appendix contains the ANSYS batch files used for the FEA of the Miura-ori and triangular-wave corrugations.

```
 1   !Title:     ShellMiura
 2   !Author:    Sean Tolman
 3   !Date:      November, 2013
 4
 5   FINISH
 6   /CLEAR
 7   FINISH
 8
 9   !/CWD,'/auto/fsb/st72/Miura/ANSYS/Shell'
10   /FILNAM,r5,1
11
12   /BEGIN
13
14      ! Define Constants
15          pi=acos(-1)
16          a = 1                    !Side length of Parallelogram
17          b = 1
18          alpha1 = 55*pi/180       !Interior angles of parallelogram
19          alpha2 = pi/2-alpha1
20          phi = 55*pi/180          !Angle of side a from horizontal
21          zeta = 2*(pi/2-phi)      !Angles used for Miura Kinematic Equations
22          psi = pi/2-alpha1
23          l = 1/25                 !Ratio used to determine hinge size
24
25          !Miura Kinematic equations
26          gamma2 =
             pi-acos((cos(zeta)-cos(alpha1)*cos(alpha2))/(sin(alpha1)*sin(alpha
             2)))
27          gamma1 =
             acos(cos(gamma2)+(sin(alpha1)*sin(alpha2)*sin(2*gamma2)**2)/(1-cos
             (zeta)))
28          theta = acos(1-cos(psi)**2*(1-cos(pi-gamma1)))
29
30          offset1 = b*cos(theta/2)        !Offsets used for Keypoint array
31          offset2 = b*sin(theta/2)
32          ndiv = 3                 !Number of divisions for Hinge
             elements(short side)
33          ndiva = 25               !Number of divisions for Panel elements
             (long side)
34
35      !Material Properties (lb, in, s)
36          E = 2.5e5                         !modulus in psi
37          t = 1/32                          !shell thickness
38          nu = 0.37                         !Poisson's Ratio
39
40          r = 0.01                          !Stiffness Ratio (Hinge/Panel)
41
42   FINISH
43
```

```
44    /PREP7
45
46        !Define Element Properties
47
48            ET,1,SHELL181                    !Panel Elements
49            R,1,t,t,t,t                      !Real constants
50            MP,EX,1,E                        !Panel Material Properties
51            MP,PRXY,1,nu
52            MP,EX,2,E*r                      !Hinge Material Properties
53            MP,PRXY,2,nu
54
55        !Define Keypoints
56
57            K,1,0,0,a*sin(phi)
58            K,2,a*cos(phi),0,0
59            K,3,a*cos(phi)+a*l,0,0
60            K,4,2*a*cos(phi)+a*l,0,a*sin(phi)
61            K,5,2*a*cos(phi)+2*a*l,0,a*sin(phi)
62            K,6,0-offset1,0+offset2,a*sin(phi)
63            K,7,a*cos(phi)-offset1,0+offset2,0
64            K,8,a*cos(phi)+a*l-offset1,0+offset2,0
65            K,9,2*a*cos(phi)+a*l-offset1,0+offset2,a*sin(phi)
66            K,10,2*a*cos(phi)+2*a*l-offset1,0+offset2,a*sin(phi)
67            K,11,0-offset1,0+offset2+a*l,a*sin(phi)
68            K,12,a*cos(phi)-offset1,0+offset2+a*l,0
69            K,13,a*cos(phi)+a*l-offset1,0+offset2+a*l,0
70            K,14,2*a*cos(phi)+a*l-offset1,0+offset2+a*l,a*sin(phi)
71            K,15,2*a*cos(phi)+2*a*l-offset1,0+offset2+a*l,a*sin(phi)
72            K,16,0,0+2*offset2+a*l,a*sin(phi)
73            K,17,a*cos(phi),0+2*offset2+a*l,0
74            K,18,a*cos(phi)+a*l,0+2*offset2+a*l,0
75            K,19,2*a*cos(phi)+a*l,0+2*offset2+a*l,a*sin(phi)
76            K,20,2*a*cos(phi)+2*a*l,0+2*offset2+a*l,a*sin(phi)
77            K,21,0,0+2*offset2+2*a*l,a*sin(phi)
78            K,22,a*cos(phi),0+2*offset2+2*a*l,0
79            K,23,a*cos(phi)+a*l,0+2*offset2+2*a*l,0
80            K,24,2*a*cos(phi)+a*l,0+2*offset2+2*a*l,a*sin(phi)
81            K,25,2*a*cos(phi)+2*a*l,0+2*offset2+2*a*l,a*sin(phi)
82            K,26,0,-a*l/2,a*sin(phi)
83            K,27,a*cos(phi),-a*l/2,0
84            K,28,a*cos(phi)+a*l,-a*l/2,0
85            K,29,2*a*cos(phi)+a*l,-a*l/2,a*sin(phi)
86            K,30,2*a*cos(phi)+2*a*l,-a*l/2,a*sin(phi)
87
88        !Define Lines
89
90            LSTR,1,2              !line 1
91            LSTR,2,7              !line 2
92            LSTR,7,6              !line 3
```

```
93            LSTR,6,1              !line 4
94            LSTR,2,3              !line 5
95            LSTR,7,8              !line 6
96            LSTR,3,4              !line 7
97            LSTR,4,9              !line 8
98            LSTR,9,8              !line 9
99            LSTR,8,3              !line 10
100           LSTR,4,5              !line 11
101           LSTR,9,10             !line 12
102           LSTR,10,5             !line 13
103           LSTR,6,11             !line 14
104           LSTR,7,12             !line 15
105           LSTR,8,13             !line 16
106           LSTR,9,14             !line 17
107           LSTR,10,15            !line 18
108           LSTR,11,12            !line 19
109           LSTR,12,17            !line 20
110           LSTR,17,16            !line 21
111           LSTR,16,11            !line 22
112           LSTR,12,13            !line 23
113           LSTR,17,18            !line 24
114           LSTR,13,14            !line 25
115           LSTR,14,19            !line 26
116           LSTR,19,18            !line 27
117           LSTR,18,13            !line 28
118           LSTR,14,15            !line 29
119           LSTR,19,20            !line 30
120           LSTR,15,20            !line 31
121           LSTR,16,21            !line 32
122           LSTR,17,22            !line 33
123           LSTR,18,23            !line 34
124           LSTR,19,24            !line 35
125           LSTR,20,25            !line 36
126           LSTR,21,22            !line 37
127           LSTR,22,23            !line 38
128           LSTR,23,24            !line 39
129           LSTR,24,25            !line 40
130           LSTR,1,26             !line 41
131           LSTR,2,27             !line 42
132           LSTR,3,28             !line 43
133           LSTR,4,29             !line 44
134           LSTR,5,30             !line 45
135           LSTR,26,27            !line 46
136           LSTR,27,28            !line 47
137           LSTR,28,29            !line 48
138           LSTR,29,30            !line 49
139
140           ALLSEL,ALL
141
```

73

```
142        !Define Areas
143            AL,1,2,3,4            !area 1
144            AL,5,10,6,2          !area 2
145            AL,7,8,9,10          !area 3
146            AL,11,13,12,8        !area 4
147            AL,3,15,19,14        !area 5
148            AL,6,16,23,15        !area 6
149            AL,9,17,25,16        !area 7
150            AL,12,18,29,17       !area 8
151            AL,19,20,21,22       !area 9
152            AL,23,28,24,20       !area 10
153            AL,25,26,27,28       !area 11
154            AL,29,31,30,26       !area 12
155            AL,21,33,37,32       !area 13
156            AL,24,34,38,33       !area 14
157            AL,27,35,39,34       !area 15
158            AL,30,36,40,35       !area 16
159            AL,1,41,46,42        !area 17
160            AL,5,42,47,43        !area 18
161            AL,7,43,48,44        !area 19
162            AL,11,44,49,45       !area 20
163
164        ! Assign Line Attributes
165
166            LSEL,S,LENGTH,,a
167            LSEL,A,LENGTH,,b
168            LESIZE,ALL,,,ndiva
169            ALLSEL,ALL
170            LSEL,S,LENGTH,,a*l
171            LESIZE,ALL,,,ndiv
172
173        !Assign Element Attributes to Areas
174
175            ASEL,S,AREA,,1,3,2
176            ASEL,A,AREA,,9,11,2
177            AATT,1,1,1
178            ASEL,INVE
179            AATT,2,1,1
180            ALLSEL,ALL
181
182        !Mesh Model
183
184            !Mesh Hinges
185            MSHKEY,1
186            MSHAPE,0,2D
187            ASEL,S,MAT,,2
188            AMESH,all
189            ALLSEL,all
190
```

74

```
191            !Mesh Panels
192            MSHKEY,0
193            MSHAPE,0,2D                      !Quad elements
194            MOPT,EXPND,4
195            MOPT,TRANS,2
196            ASEL,S,MAT,,1
197            AMESH,all
198            ALLSEL,all
199
200        !Copy Areas
201
202            ASEL,S,LOC,Y,0,5
203            AGEN,5,ALL,,,0,2*(offset2+a*l),0,0,0,0          !Number of unit
               cells in y-dir
204            ASEL,ALL
205            AGEN,5,ALL,,,2*a*(cos(phi)+l),0,0,0,0,0          !Number of unit
               cells in x-dir
206            ASEL,ALL
207            AGEN,2,ALL,,,-10*a*(cos(phi)+l),0,0,0,0,0        !Doubles pattern
               in x-dir (-6 is multiple of x dir unit cells and 2)
208            !ASEL,ALL                                        !Not needed if
               using symmetry BC
209            !AGEN,2,ALL,,,0,-6*(offset2+a*l),0,0,0,0
210            ALLSEL,ALL
211            NUMMRG,NODE                                      !Merge
               coincident nodes and KP
212            NUMMRG,KP
213
214    FINISH
215
216    /SOL
217
218        !Apply Boundary Conditions/Loads
219
220            KSEL,S,LOC,Z,-0.5*a,0.01*a              !"Table top" boundary
               condition
221            DK,ALL,UZ,0
222            ALLSEL,ALL
223
224            NSEL,S,LOC,Y,-a*l/2                     !Symmetry boundary
               condition, X-Z plane
225            D,ALL,UY,0
226            D,ALL,ROTX,0
227            D,ALL,ROTZ,0
228            ALLSEL,ALL
229
230            NSEL,S,loc,y,0                          !Apply displacement
               across hinge
231            NSEL,R,loc,x,0,-a*l
```

```
232          CM,lapp,NODE
233          ALLSEL,all
234
235          D,lapp,UX,0                          !Fix KP 1 in X
236          D,lapp,UY,0
237
238          D,lapp,UZ,-0.01                      !Apply disp. load to KP
             1, load step 1
239          SOLCONTROL,ON
240          NSUBST,5,20,1
241          KBC,0
242          OUTRES,all,1
243          lswrite,1
244
245          D,lapp,UZ,-0.05                      !Load step
             2
246          SOLCONTROL,ON
247          NSUBST,5,50,5
248          KBC,0
249          OUTRES,all,1
250          lswrite,2
251
252          D,lapp,UZ,-0.1                       !Load step 3
253          SOLCONTROL,ON
254          NSUBST,10,50,10
255          KBC,0
256          OUTRES,all,1
257          lswrite,3
258
259          D,lapp,UZ,-.3                        !Load step 4
260          SOLCONTROL,ON
261          NSUBST,20,50,10
262          KBC,0
263          OUTRES,all,1
264          lswrite,4
265
266          ANTYPE,0
267          LSSOLVE,1,4,1                        !Solve load steps
268
269    FINISH
270        /DSCALE,1,1.0
271
272    /POST1
273
274        KSEL,s,loc,z,a*sin(phi)
275        NSLK,s,1
276        NLIST,ALL,COORD
277        PRNSOL,U,SUM
278        ALLSEL,ALL
```

```
279
280        KSEL,s,loc,z,0
281        NSLK,s,1
282        NLIST,ALL,COORD
283        PRRSOL,FZ
284        ALLSEL,ALL
285
286    FINISH
287
288    /POST26
289
290        KSEL,s,kp,,1
291        NSLK,s
292        *get,nk2,node,0,num,max
293        ALLSEL,all
294
295        KSEL,s,KP,,1177
296        NSLK,s
297        *get,nk3,node,0,num,max
298        ALLSEL,all
299
300        NSOL,2,nk2,U,Z,uz2              !Z deflection of node at
           keypoint 1
301        RFORCE,3,nk2,F,Z,fz2           !Reaction forces of node at
           keypoint 1
302        NSOL,4,nk3,U,Z,uz1177          !Z deflection of node at
           keypoint 1177
303        RFORCE,5,nk3,F,Z,fz1177        !Reaction forces of node at
           keypoint 1177
304
305    FINISH
306
307
308
```

```
1   !Title:      ShellWave
2   !Author:     Sean Tolman
3   !Date:       January, 2014
4
5   FINISH
6   /CLEAR
7   FINISH
8
9   !/CWD,'/auto/fsb/st72/Miura/ANSYS/Shell'
10  /FILNAM,W_r01,1
11
12  /BEGIN
13
14      !Define Constants
15          pi=acos(-1)
16          a = 1                    !Side length of Wave
17          b = 0.7438                   !Width of wave
18          phi = 55*pi/180          !Angle of side a from horizontal
19          l = 1/25                 !Ratio used to determine panel hinge width
20          ndiv = 3                 !Number of divisions for Hinge
            elements(short side)
21          ndiva = 10               !Number of divisions for Panel elements
            (long side)
22
23      !Material Properties (lb, in, s)
24          E = 2.5e5                           !modulus in psi
25          t = 1/32                            !shell thickness
26          nu = 0.37                           !Poisson's Ratio
27
28          r = 0.5                             !Stiffness Ratio (Hinge/Panel)
29
30  FINISH
31
32  /PREP7
33
34      !Define Element Properties
35
36          ET,1,SHELL181                    !Panel Elements
37          R,1,t,t,t,t                      !Real constants
38          MP,EX,1,E                        !Material 1, Panel Material
            Properties
39          MP,PRXY,1,nu
40          MP,EX,2,E*r                      !material 2, Hinge Material
            Properties
41          MP,PRXY,2,nu
42
43      !Define Keypoints
44
45          K,1,0,0,a*sin(phi)
```

78

```
46          K,2,a*l,0,a*sin(phi)
47          K,3,a*cos(phi)+a*l,0,0
48          K,4,a*cos(phi)+2*a*l,0,0
49          K,5,2*a*cos(phi)+2*a*l,0,a*sin(phi)
50          K,6,0,b,a*sin(phi)
51          K,7,a*l,b,a*sin(phi)
52          K,8,a*cos(phi)+a*l,b,0
53          K,9,a*cos(phi)+2*a*l,b,0
54          K,10,2*a*cos(phi)+2*a*l,b,a*sin(phi)
55
56     !Define Lines
57
58          LSTR,1,2              !line 1
59          LSTR,2,7              !line 2
60          LSTR,7,6              !line 3
61          LSTR,6,1              !line 4
62          LSTR,2,3              !line 5
63          LSTR,7,8              !line 6
64          LSTR,3,4              !line 7
65          LSTR,4,9              !line 8
66          LSTR,9,8              !line 9
67          LSTR,8,3              !line 10
68          LSTR,4,5              !line 11
69          LSTR,9,10             !line 12
70          LSTR,5,10             !line 13
71          ALLSEL,ALL
72
73     !Define Areas
74
75          AL,1,2,3,4           !area 1
76          AL,5,10,6,2          !area 2
77          AL,7,8,9,10          !area 3
78          AL,11,13,12,8        !area 4
79
80     !Assign Line Attributes
81
82          LSEL,S,LENGTH,,a
83          LESIZE,ALL,,,ndiva                    !Divisions for Short Side of
               Panel
84          ALLSEL,ALL
85          LSEL,S,LENGTH,,b                      !Divisions for Long Side of
               Panel
86          LESIZE,ALL,,,ndiva*b
87          ALLSEL,ALL
88          LSEL,S,LENGTH,,a*l                    !Divisions for Short Side of
               Hinge
89          LESIZE,ALL,,,ndiv
90          ALLSEL,ALL
91
```

```
 92        !Assign Element Attributes to Areas
 93
 94            ASEL,S,AREA,,2,4
 95            AATT,1,1,1
 96            ASEL,INVE
 97            AATT,2,1,1
 98            ALLSEL,ALL
 99
100        !Mesh Model
101
102            !Mesh Hinges
103            MSHKEY,1
104            MSHAPE,0,2D
105            ASEL,ALL
106            AMESH,all
107            ALLSEL,all
108
109            !Mesh Panels
110            !MSHKEY,1
111            !MSHAPE,0,2D                        !Quad elements
112            !ASEL,S,MAT,,1
113            !AMESH,all
114            !ALLSEL,all
115
116        !Copy Areas
117
118            ASEL,S,LOC,Y,0,5
119            AGEN,10,ALL,,,0,b,0,0,0,0                              !Number of unit
               cells in y-dir
120            ASEL,ALL
121            AGEN,5,ALL,,,2*(a*cos(phi)+l*a),0,0,0,0,0        !Number of unit
               cells in x-dir
122            ASEL,ALL
123            AGEN,2,ALL,,,-10*(a*cos(phi)+l*a),0,0,0,0,0      !Doubles pattern
               in x-dir (-6 is multiple of x dir unit cells and 2)
124            ALLSEL,ALL
125            NUMMRG,NODE                                              !Merge
               coincident nodes and KP
126            NUMMRG,KP
127
128    FINISH
129
130    !/EOF
131
132    /SOL
133
134        !Apply Boundary Conditions/Loads
135
136            KSEL,S,LOC,Z,0                !"Table top" boundary condition
```

```
137        DK,ALL,UZ,0
138        ALLSEL,ALL
139
140        NSEL,S,LOC,Y,0                        !Symmetry boundary
           condition, X-Z plane
141        D,ALL,UY,0
142        D,ALL,ROTX,0
143        D,ALL,ROTZ,0
144        ALLSEL,ALL
145
146        NSEL,S,loc,y,0                        !Apply displacement
           across hinge
147        NSEL,R,loc,x,0,a*l
148        CM,lapp,NODE
149        ALLSEL,all
150
151        D,lapp,UX,0                           !Fix KP 1 in X
152        D,lapp,UY,0
153
154        D,lapp,UZ,-0.01                       !Apply disp. load to KP
           1, load step 1
155        SOLCONTROL,ON
156        NSUBST,5,20,1
157        KBC,0
158        OUTRES,all,1
159        lswrite,1
160
161        D,lapp,UZ,-0.05                       !Load step
           2
162        SOLCONTROL,ON
163        NSUBST,5,50,5
164        KBC,0
165        OUTRES,all,1
166        lswrite,2
167
168        D,lapp,UZ,-0.1                        !Load step 3
169        SOLCONTROL,ON
170        NSUBST,10,50,10
171        KBC,0
172        OUTRES,all,1
173        lswrite,3
174
175        D,lapp,UZ,-.3                         !Load step 4
176        SOLCONTROL,ON
177        NSUBST,20,50,10
178        KBC,0
179        OUTRES,all,1
180        lswrite,4
181
```

```
182         ANTYPE,0
183         LSSOLVE,1,4,1                              !Solve load steps
184
185   FINISH
186
187   /DSCALE,1,1.0
188
189   /EOF
190
191   /POST1
192
193       KSEL,s,loc,z,0
194       NSLK,s,1
195       NLIST,ALL,COORD
196       PRRSOL,FZ
197       ALLSEL,ALL
198
199   FINISH
200
201   /POST26
202
203       KSEL,s,kp,,1
204       NSLK,s
205       *get,nk1,node,0,num,max
206       ALLSEL,all
207
208       KSEL,s,KP,,2
209       NSLK,s
210       *get,nk2,node,0,num,max
211       ALLSEL,all
212
213       NSOL,2,nk1,U,Z,uz1                  !Z deflection of node at
          keypoint 1
214       RFORCE,3,nk1,F,Z,fz1               !Reaction forces of node at
          keypoint 1
215       NSOL,4,nk2,U,Z,uz2                  !Z deflection of node at
          keypoint 2
216       RFORCE,5,nk2,F,Z,fz2               !Reaction forces of node at
          keypoint 2
217
218       PRVAR,2,3,4,5
219
220   FINISH
221
222
223
```

APPENDIX B.   CRASH PAD PROJECT FINAL REPORT

The following pages are comprised of the final report for a design project completed from May to August of 2013. This *Summer Burst Project*, sponsored by the BYU Compliant Mechanisms Research Group was supervised by Terry Batemen and lead by Sean Tolman with team members Jessica Morgan, Gary Ellignson, Greg Belnap and Mary Wilson.

CMR Summer Burst Project
Energy Absorbing
Final Report

1. Introduction/Motivation

Bouldering is a form of rock climbing where the climbers, rather than trying to scale a high rock face or mountain, focus on difficult and technical climbing challenges that are closer to the ground. Bouldering routes typically reach no more than 10 to 20 feet above the ground and the most difficult part of the route is often just a few feet off the ground. Because of this, climbers typically do not use ropes or harnesses while bouldering. To protect themselves from injury due to falls, climbers place large foam pads, called "crash pads", on the ground below them as they climb.

Several types of crash pads are available on the market for bouldering. All of these crash pads use the same basic design of utilizing heavy foam pads to absorb the energy of a fall. These foam pads are effective for the energy absorption involved in a bouldering fall but have several inconvenient drawbacks. Many bouldering locations are remote and only accessible by hiking, requiring climbers to carry the crash pad to the climbing site. The heavy foam used in crash pads is not easily compressed or compactable, making it awkward to transport to the climbing site and challenging to store in between use. The Tessapad is designed to be a reliable crash pad comparable to those on the market with the benefit of being able to compress to half of its fully deployed size. The compactability of the Tessapad makes it ideal for transporting to and from the climbing site and storing in between use with the same injury protection of a traditional crash pad.

1.1 Design Requirement Goals

The Tessapad needs to match or outperform current marketed crash pads in the areas of cushioning a person's fall, durability, transportability, easy compaction and deployed stability in order to make it a viable product. A statement on each of these features meeting customer's needs is as follows:
1. The pad needs to cushion a person's fall by decreasing momentum.
2. The pad needs to be able to sustain repeated falls without performance loss.
3. The pad needs to be lighter and—when compressed—more compact than the leading crash pad.
4. The pad needs to be easily re-compressed once deployed.
5. The pad needs to be stable in its deployed state.

Each of these features are important to the design of the Tessapad to make it a marketable crash pad.

There is currently no set standard for bouldering crash pads specifying the energy absorbing properties of the pad. Thus, crash pads readily on the market were used to set quantified energy absorption, density and weight benchmarks for the Tessapad, which are related in Table 1.

To determine the energy absorption benchmark, drop tests were done on a current commercially available crash pad using a 6.35 kg (14 lb) bowling ball. The crash pad was placed on top of a force plate to measure force over time and deflection. The bowling ball was dropped from a height of 2.13 m (7 ft.) The results of these tests are reflected in Figure 1

Table 1 - Crash Pad Design Metrics

| Need	Metric	Units	Test	Values
Cushioned Fall	Acceleration	m/s^2	Measure the acceleration that occurs when landing on the pad using force plates and a bowling ball.	See Figs 1 and 2.
Durability	Acceleration Deviation	$\% \ m/s^2$	Subject the pad to 10 repeated impacts. Using force plates, measure for any deviation in acceleration after each use.	< 20% acceleration deviation
Transportability	Density	lb/ft^3	Determine the ratio of the pad's weight to both its deployed and un-deployed size.	Deployed: $< 3lbs/ft^3$
	Size	ft^3	Measure the pad size in its deployed state, and then measure the pad's size in its compacted state.	Compacted size 50% of deployed size
Easy Compaction	Compression Force	lbs	Using spring scales, measure the necessary force for keeping the pad in its fully-compressed state.	<5lbs
Deployed Stability	Pass/Fail	N/A	Observe if the pad remains fully deployed under no external loads.	N/A

Force Deflection Curve
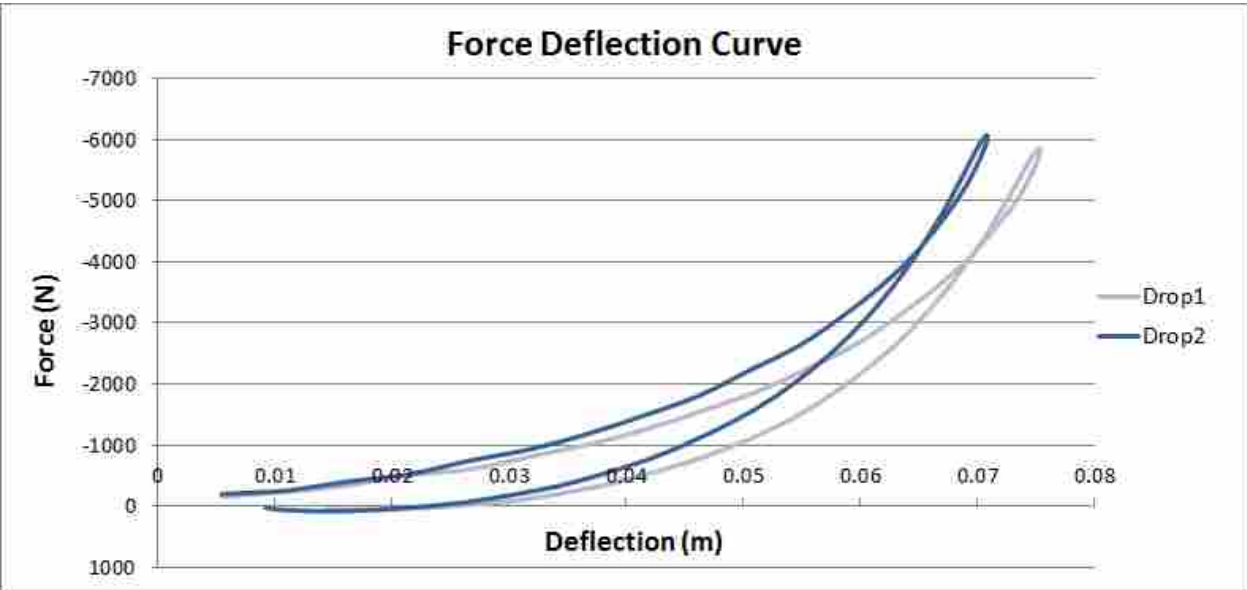
Figure 1- The force deflection curve, the displacement (meters) of the pad versus the force (Newtons) in the drop test.

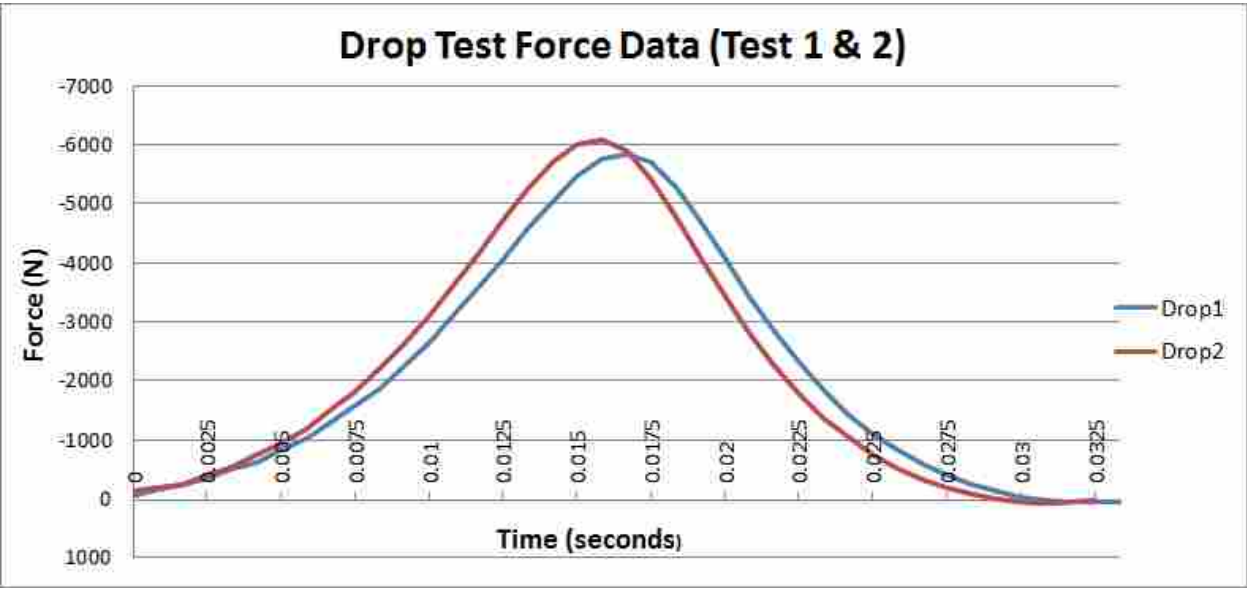**Drop Test Force Data (Test 1 & 2)**

Figure 2 - The force (Newtons) over time (seconds) in the drop test.

showing the force deflection curve and Figure 2 showing the drop test force data. Both Fig 1 and Fig 2 show that the pad needs to be capable of withstanding 6000 N of force without bottoming out. The Tessapad needs to respond similarly to this tested crash pad under a dymanic load.

These outlined design requirements will make the Tessapad a competitive product in the market of bouldering crash pads by meeting the basic need of energy absorption and the added benefits of compactability that have never been applied before to crash pads.

2. Concepts

Our prototype utilizes the Miura-ori, an origami fold pattern invented by Japanese astrophysicist, Koryo Miura. The Miura-ori pattern consists of parallelograms, as shown in Figure 3, connected with mountain and valley folds on all four sides. A plastic version of Miura-ori uses living hinges to connect the parallelograms and provide movement. Miura-ori has distinct properties beneficial to energy absorption. Any downward force on the Miura-ori plastic layer is translated into planar expansion of the material in two orthogonal directions.
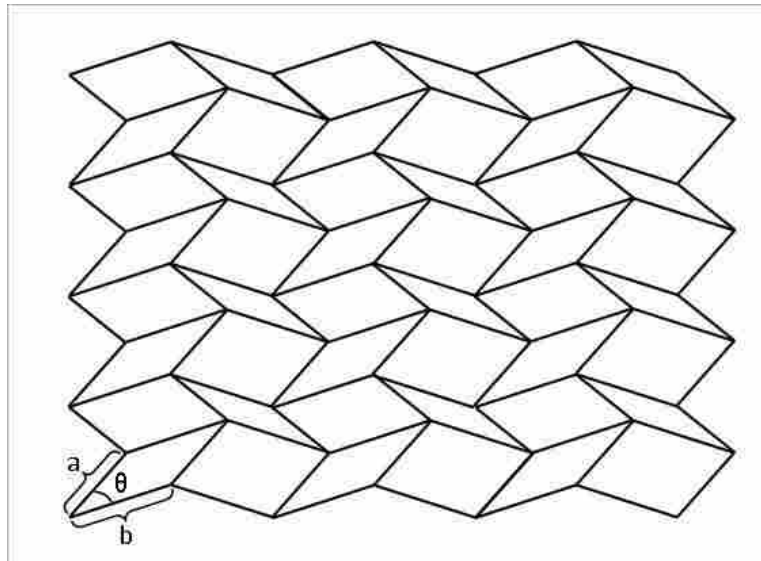

Figure 3- Top view of Miura-ori pattern

The main concept of the Tessapad is to exploit the kinematic properties of the Miura-ori. It is designed to have comparable energy absorption to current marketable crash pads with the added benefit of compactability. This rules out the traditional use of foam as the energy absorber as it is heavy, bulky and does not easily compress. Using innovative design methods inspired by origami the Tessapad takes a different approach, combining energy absorption and compactability into the same features.

The Tessapad utilizes multiple layers of the Miura-ori pattern stacked on top of each other as shown in Figure 4. Each layer is fastened to a flat, elastic membrane which serves as the main mechanism for absorbing the energy placed on the pad. Upon impact, the Miura-ori pattern expands and the elastic membrane absorbs the energy and provides some padding. The use of multiple layers allow the pad to be thick while each individual layer has a relatively small tessellation pattern. The layers also allow multiple membranes to be used in absorbing the energy needed.

The actual kinematic properties of the Miura-ori are dependent on a set of input variables such as the size and angle of each parallelogram in the overall pattern. The optimization of these variables best suited for energy absorption will be discussed in the optimization section.
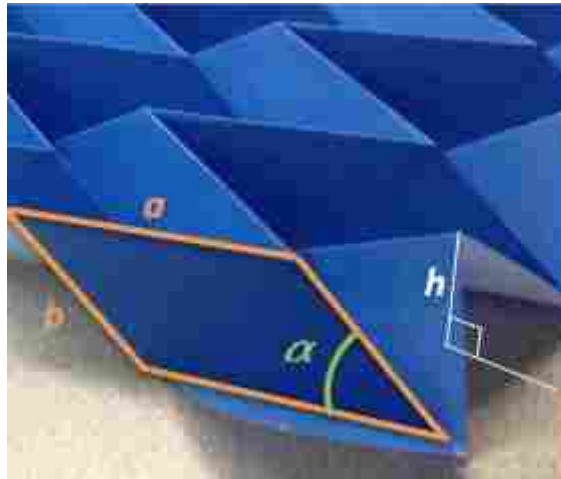
Figure 4 - Parameters of the Miura-ori tessellation.

3. Optimization

A mathematical model was developed for the energy absorption of a Miura-ori unit cell and the attached membrane. The model was developed by considering the Miura-ori unit cell to be a spherical mechanism and the attached membrane to be two orthogonal linear springs. A virtual work analysis was applied to determine the work done by a force orthogonal to the plane of the Miura-ori. See Appendix 7.5 for the mathematical model. As mentioned, the Miura-ori is a tessellation of parallelograms that are defined by the length of their adjacent sides a and b and the acute interior angle between them, α as shown in Figure 4. For given side lengths of $a =$1.25" and $b =$1.5", the model was used to find the interior angle, α, that results in the maximum total work energy for the compression of the unit cell. It was found that an acute interior angle (α in Figure 6) of about 55 degrees would yield the most energy absorption. The parallelogram side lengths were chosen based on the desired dimensions for the final prototype and, according to the model, were not critical to maximizing the energy absorption. The height h was chosen to achieve a planar compaction of the sheet of 50%.

4. Product

The living hinges as joints in the material make it plausible for the Miura-ori to maintain its properties of motion and durability
The current design utilizes 1/16" polypropylene as the plastic for the Miura-ori layers. The plastic sheet was folded after living hinges that were cut into the material. The living hinges were cut on a CNC mill using a 1/16" ball end mill. Optimally the living hinges in polypropylene would be cut down to leave them about .008" thick. However, because of the size of the end prototype there are inaccuracies inherent in cutting this relatively large sheet in a mill, the hinges were approximately .020 $\pm$ .015".
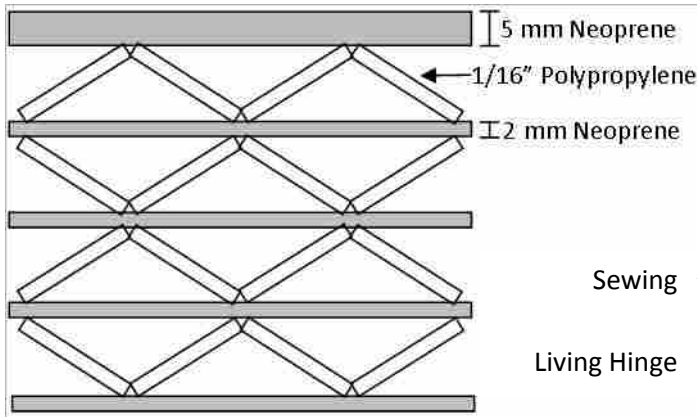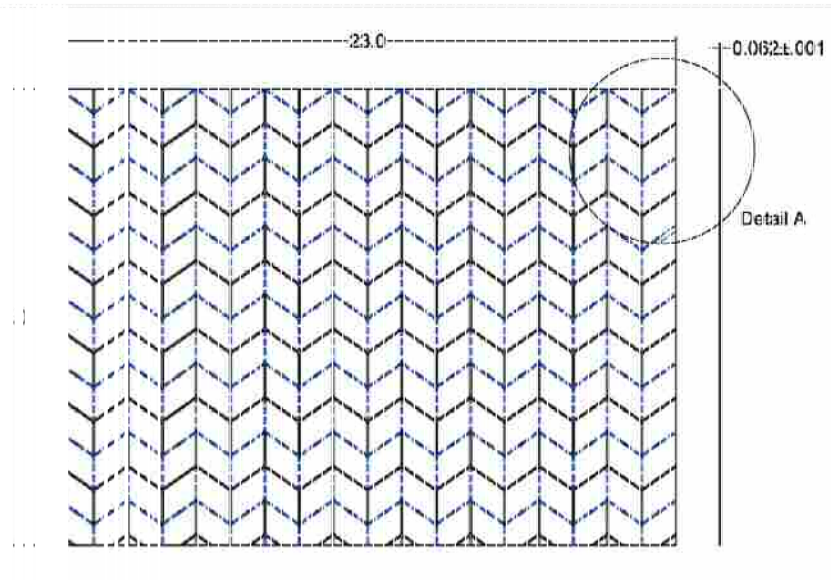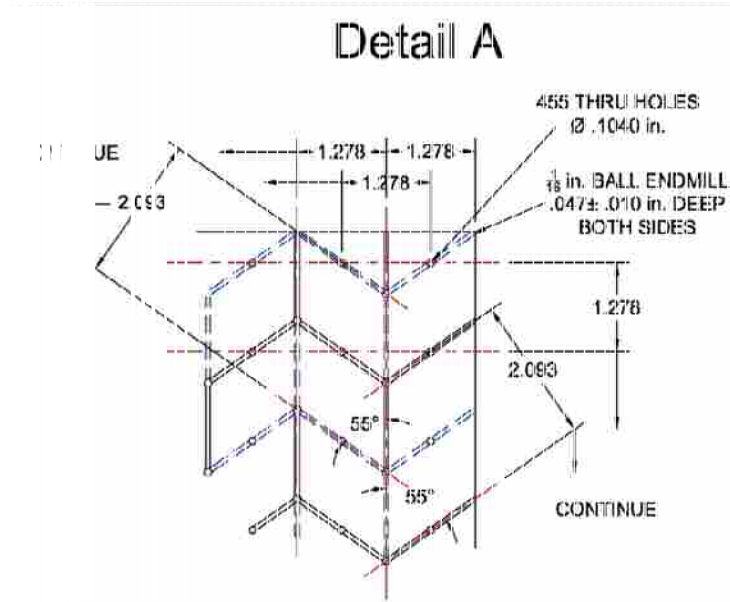
Figure 5 – Drawing of crash pad layering

Figure 6 – Side view of crash pad design showing layering of Miura-ori and elastic membrane.

The Miura-ori layers are stacked such that a valley in one layer is fastened to the mountain of the proceeding layer. They are separated only by the elastic membrane. In the prototype, the elastic membrane is made up of 2 mm thick neoprene. The layers of neoprene and polypropylene Miura-ori are attached using sewing. Holes are punched in the hinges of the Miura-ori pattern using an industrial sewing machine to facilitate sewing the layers together. A layer of 5 mm thick neoprene is fastened to the top surface of the pad to provide extra padding upon impact.

Detail A

455 THRU HOLES
Ø .1040 in.

UE

— 2.093

1.278 — 1.278

1.278

⅛ in. BALL ENDMILL
.047± .010 in. DEEP
BOTH SIDES

1.278

2.093

55°

55°

CONTINUE

5. Results

During assembly of the pad it was discovered that the thick hinges were to stiff to fold and move. For this reason several of the hinges were cut and taped with Duct Tape. See Appendix 7.1.1 for more details.

In an initial pretest, just after assembly was complete, one of the middle layers became inverted, see appendix 7.1.3.

Testing was done on the 14" by 19.75" prototype to verify the energy absorption of the pad and compare it to the aforementioned tests done on a standard crash pad. The tested prototype consists of only 3 layers due to the difficulty of fastening the layers. The prototype Tessapad was tested in the same manner by placing it on a force plate and dropping a 6.35 kg (14 lb) bowling ball from a height of 2.13 m (7ft). The test bowling ball bottomed out and experienced an acceleration force of 11000 N, twice the acceleration force of the benchmark for a standard crash pad. The test was unable to be repeated due to the limitations of the prototype and force plate, therefore it was impossible to test deviations in the acceleration for repeated drops. As for the other set benchmarks, the Tessapad has a density of 6.99 lb/ft^3 and it requires > 5lbs for compression to its compacted state. On the other hand the Tessapad is 50-60% compactable and is stable in its deployed state. The current prototype does not meet all of our desired goals on the performance metrics, but it is highly compactable and shows potential for energy absorption.

Section of results of the drop test. Maybe a plot of the data like the one in the goals section…

90

After the testing was completed the prototype was examined. It was found that the bistable inverting accrued where the bowling ball had impacted, and failures in the hinges were also visible. See the figures below.
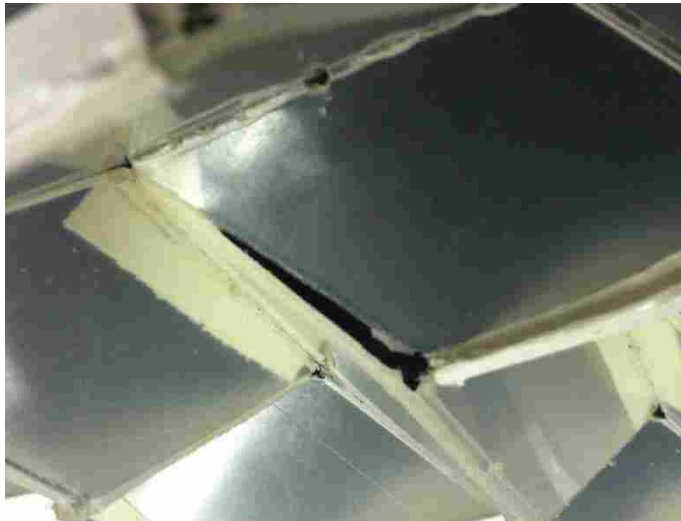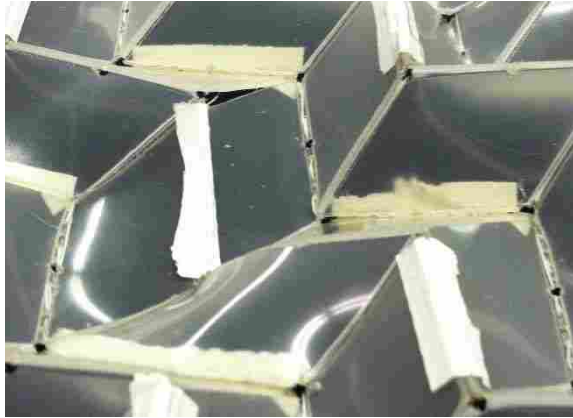
6. Conclusion

The current Tessapad prototype does not meet all the desired metrics as described in Table 1. The Tessapad prototype did not sufficiently accelerate a load, is not durable, the density is twice as that of the average crash pad,and requires larger than projected force for compression. On the plus side the Tessapad is stable in its deployed state and overshoots the benchmark for compactability at being able to compress 50-60% of its deployed state.

Many of the variables in the Tessapad design that affect these metrics are adjustable and need to be modified in the right combination to make to pad work for it desired function. There seems to be several tradeoffs that still need to be looked at. For example, increased joint strength and increased compactibility are two desired improvements for future prototypes but they seems two require opposite actions. Increasing the joint strength requires that the joints be make thick enough not to break but decreasing the force to compact the pad to make it more compactible requires thinner, more flexible joint. Please see the appendix for more tradeoffs to be solved.

Further research is needed to solve the above mentioned tradeoffs and to select material to make it more lightweight and efficient, hinge type to improve energy absorption and compression force, fastening methods to make it more durable and easier to manufacture. Still the miura ori pattern shows great potential as a compactable energy absorber with the correct implementation. In conclusion, the Tessapad's method of using a combination of miura ori and elastic membrane layers has not been eliminated as viable energy absorber and further research is needed.

7. Appendix

7.1 Challenges

Many challenges presented themselves during the design of the Tessapad including the hinge selection and implementation, constructing the Miura-ori design and achieving energy absorption.

7.1.1 Hinges

Hinges are used to mimic the folds of Miura-ori pattern in paper. Many different types of hinges are possible in the design to give the necessary shape of Miura-ori. The hinges in the Tessapad need to be able to move through a full range of motion thus living hinges were selected. Living hinges provide ease of motion and are simpler to fabricate with limited facilities. Fabricating the living hinges in the Miura-ori pattern still proved to be difficult. For the Tessapad, the hinges needed to be about eight thousandths of an inch thick in order to be a true living hinge. The machine of choice to provide the most accuracy was a CNC mill. Despite the CNC mill's capabilities, tolerances were only able to create hinges between twenty and thirty thousandths of an inch, causing the hinges to be much thicker and stiffer than desired.

7.1.2 Construction

Early on, it was discovered that the Miura-ori pattern exhibited more desirable motion when stacked in multiple layers as seen in Figure 4. The resulting challenge was how to attach multiple layers. With two layers, attachment is simple by sewing corresponding ridges together. When attaching three or more layers together, conventional sewing becomes difficult. Some considerations in solving this problem included the use of rivets and even velcro between layers. For the Tessapad prototype, the use of a curved hook needle was necessary to attach subsequent layers. Other fastening methods were considered but not possible to implement with limited time and resources.

7.1.3 Bistable Buckling

Another difficulty of the Miura-ori pattern is buckling. The living hinges in the Miura-ori pattern form bistable cells, making it possible for the mountains in the pattern to pop into

valleys. Once in its other stable state it is difficult to push back into its original stable position especially when stacked in layers. The buckling also makes it difficult to compact. Buckling factors should be implemented into the design of the crash pad.

7.2 Material Selection

7.2.1 Miura-ori layer

The Tessapad is an application that requires materials to be strong and flexible; in choosing the material for the Miura-ori pattern, polymers seemed the most likely candidates. Because the design employs the use of living hinges, polypropylene is our best choice due to its high fatigue limit.

7.2.2 Elastic Membrane layer

When the design included the use of an elastic membrane, fabrics took precedent over rubbers and foams because it was known that the Miura-ori layers would be attached by sewing. In early tests, fabrics with high elasticity (such as spandex) were considered but were ultimately discarded because the material stretched easily under minimal tensile forces. After further research, neoprene fabric (the primary material used in wetsuits) seemed to offer good stretch coupled with strength under tensile loads and became our primary membrane for prototyping.

Instron tests were performed on the neoprene fabric to determine its modulus of elasticity and if it would be a suitable energy absorber in our application. The average modulus found from the tests from our 2 mm thick neoprene fabric was 0.1151075 MPa. However, neoprene fabric is not perfectly elastic; each time the fabric is stretched, its shape deforms slightly, effectively losing some of its stretch with each use. As such, further material investigation is needed in finding a suitable membrane material for the Tessapad.

7.3 Manufacturing Ideas

There are several possible solutions to manufacturing the Tessapad that will help to overcome some of the challenges presented previously. As for the polypropylene etched with the Miura-ori pattern, conventional machining proved too inaccurate and time consuming to create effective living hinges. Injection molding also seems unlikely due to the pad's necessary size and features. A plausible solution is to heat the polypropylene then stamp or roll the desired shapes. This method is more time efficient and makes other hinges types possible for the design of the pad.

These are some possible manufacturing ideas for producing the Miura-ori pattern of parallelogram. Creating a manufacturing process will help with the design and functionality of the crash pad, making it a very marketable product.

7.4 Assembly Ideas

Another manufacturing difficulty is attaching multiple layers of polypropylene and elastic membrane together. During development, the use of one-sided push rivets were considered. This was not a feasible option for prototyping because the large and flat rivet heads impeded the folding motion of the Miura-ori. However, in actual fabrication, special push rivets could be developed with heads made to conform and move along with the folded polypropylene. Another possible method of attaching the layers, is to place ears in the polypropylene layers where the rivets can be placed. For more information see *Memo to Terri 8-12-13.*
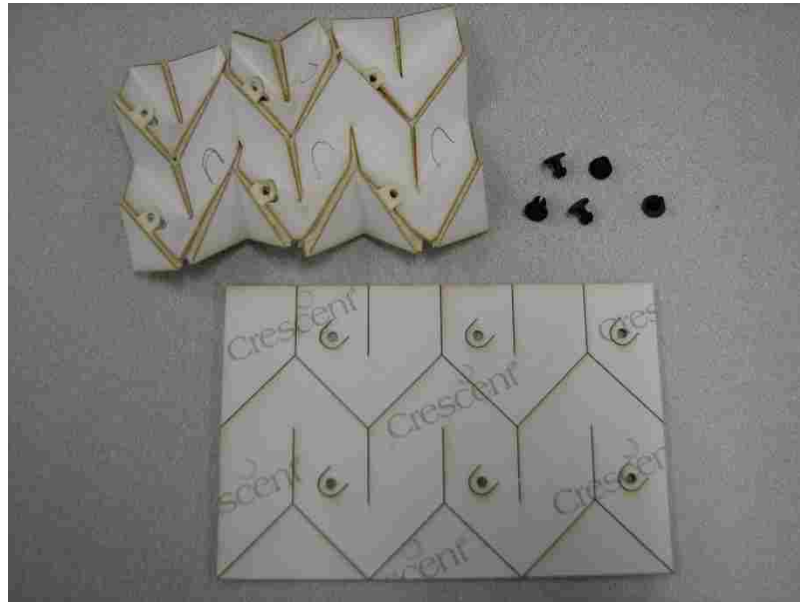
7.5 Mathematical Model

7.5.1 Kinematic Model for Miura-ori Unit Cell

$$\gamma_2 = \pi - acos\left[\frac{cos\zeta - cos\alpha_1 cos\,\alpha_2}{sin\alpha_1 sin\alpha_2}\right]$$

$$\zeta = 2acos\left(\frac{h}{a}\right)$$

$$\gamma_1 = acos\left[cos\gamma_2 + \frac{sin\alpha_1 sin\alpha_2 sin^2\gamma_2}{1 - cos\zeta}\right]$$

$$L_1 = 2asin\left(\frac{\zeta}{2}\right)$$
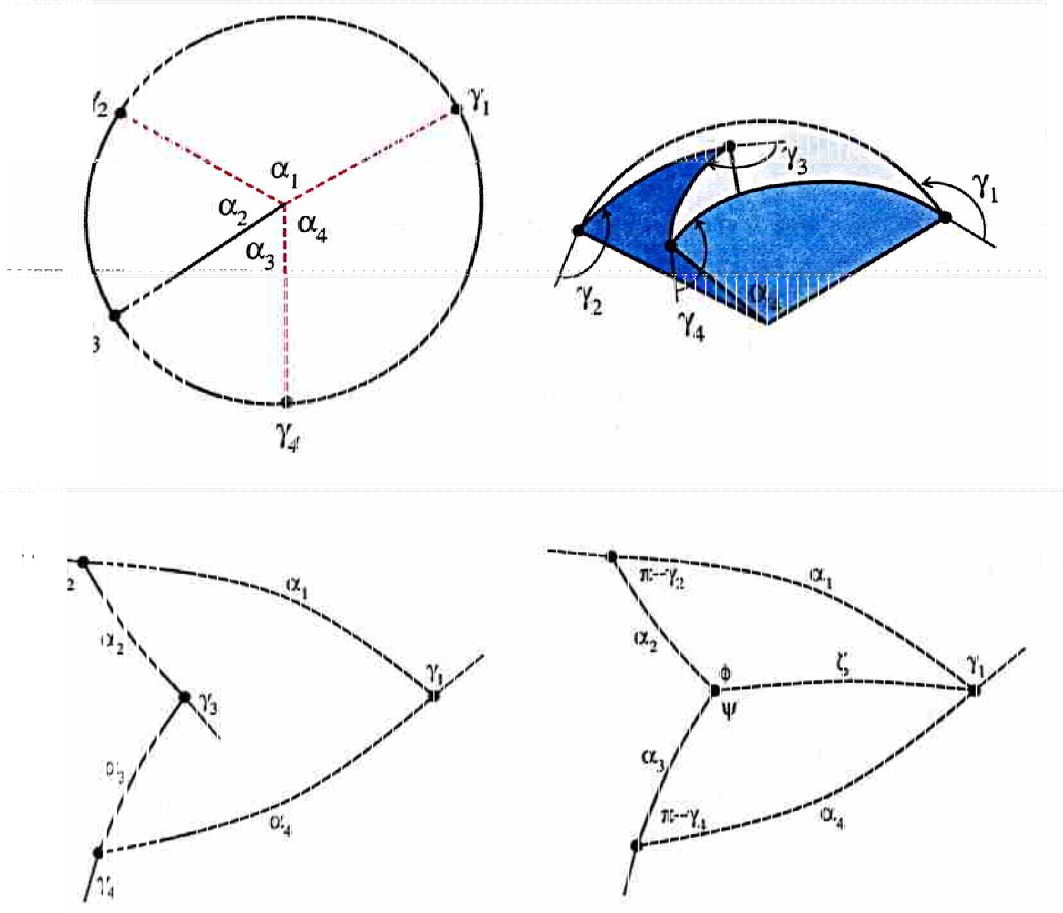
$$L_2 = 2bsin\left(\frac{\theta}{2}\right)$$

Figure 9 – Labeling of dihedral angles. (From Robert Lang Manuscript)

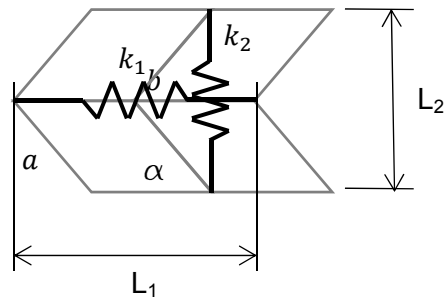## 7.5.2 Energy Model for Miura-ori Unit Cell with Membrane

Figure 10 – Parameters for Energy Model Based on Virtual Work Model

$$F = \left(\frac{dh}{d\zeta}\right)^{-1}\left(-k_1(L_1 - L_{1o})\frac{dL_1}{d\zeta} - k_2(L_2 - L_{2o})\frac{dL_2}{d\zeta}\right)$$

$$\frac{dL_1}{d\zeta} = a * cos\left(\frac{\zeta}{2}\right)$$

$$\frac{dL_2}{d\zeta} = b * cos\left(\frac{\theta}{2}\right)\frac{d\theta}{d\zeta}$$

$$\frac{d\theta}{d\zeta} = \frac{1}{\sqrt{1 - cos^2\theta}}\left(cos^2\phi\left(sin(\pi - \gamma_1)\right)\frac{d\gamma_1}{d\zeta} + \left(1 - cos(\pi - \gamma_1)\right)\right)$$

7.6 Future Tradeoffs

- o Joint strength and compactability
- o Optimal deployed angle
- o Strength and weight